A repeatable change detection approach to map extreme storm-related damages caused by intense surface runoff based on optical and SAR remote sensing: Evidence from three case studies in the South of France.

Arnaud Cerbelaud, Laure Roupioz, Gwendoline Blanchet, Pascal Breil, Xavier Briottet

ISPRS Journal of Photogrammetry and Remote Sensing 182 (2021) 153–175

Contents lists available at ScienceDirect

ISPRS Journal of Photogrammetry and Remote Sensing

journal homepage: www.elsevier.com/locate/isprsjprs

A repeatable change detection approach to map extreme storm-related damages caused by intense surface runoff based on optical and SAR remote sensing: Evidence from three case studies in the South of France

Arnaud Cerbelaud [a,b,c,*], Laure Roupioz [a], Gwendoline Blanchet [b], Pascal Breil [c], Xavier Briottet [a]

[a] ONERA, DOTA, Université de Toulouse, F-31055 Toulouse, France
[b] Centre National d'Etudes Spatiales (CNES), EO Lab, 31400 Toulouse, France
[c] Institut National de Recherche pour l'Agriculture, l'Alimentation et l'Environnement (INRAE), UR RiverLy, 69100 Villeurbanne, France

ARTICLE INFO

Keywords:
Sentinel-2
Sentinel-1
Intense rainwater runoff
Flood damage
Change detection
Supervised classification

ABSTRACT

Most flood hazards are induced either by river overflowing or intense overland flow following heavy rainfall, causing land surface damages under many forms. Until now, fine-scale detection of damages caused by intense rainwater runoff beyond the direct vicinity of major waterways has been scarcely explored using satellite remote sensing. In this work, three extreme storms in the *Aude* and *Alpes-Maritimes* departments in the South of France were investigated based on ground truths and very high resolution optical imagery (*Pléiades* satellite, IGN *orthophotos*). Plot delineation and land use information were combined to high revisit frequency and high resolution optical (Sentinel-2) and SAR (Sentinel-1) open-source data to test a simple automatic and replicable change detection method to locate damaged plots using supervised classification. Based on a unique training sample from the *Aude* floods of October 2018, combinations of plot-based spectral indicators allowed reaching overall detection accuracies greater than 85% on independent validation samples for all three events. A simple land use inter-class demeaning pre-processing used to account for land-specific seasonal variations improved event and site repeatability by lowering false detection rates down to a maximum of 13%. The benefits of introducing SWIR channel in addition to visible and near-infrared indices were limited to a few percentage points. SAR-derived proxies of soil moisture and roughness in weakly vegetated areas were consistent with the presence of degradations, with VV being the most sensitive polarization. However, classification accuracy was not significantly increased with Sentinel-1 data as compared to the exclusive use of Sentinel-2. Additional tests revealed that should the closest available optical images be rather distant in time because of persistent cloud cover, the method is reasonably robust as long as stable ground conditions were observed before the event. The need for images close in time was however emphasized through cross-site training. Indeed, efficient replicability from one site to another relied on using unaffected learning plots with slightly more inherent variability in time variations of spectral indices compared to the test site. Beyond the investigation of three case studies, this work demonstrates the performance and repeatability potential of a new probabilistic change detection method to expose various kinds of extreme rainfall-related disturbances, in particular those occurring far from the main hydrographic network. Should spatially accurate rainfall products be available, comprehensive mapping of intense stormwater runoff hazards using this original plot-based approach will then allow improving the understanding of overland flow generation mechanisms in hydrological models.

1. Introduction

Flooding events are mostly triggered by overland rainwater flow following extreme storms. Depending on rainfall magnitude, rate or duration but also on watershed configuration, land cover, pedological and lithological characteristics, hydrological consequences may vary and persist over different time scales from hours to weeks (Bell and Kar, 1969). During such events, surface runoff can materialize in various places, with water running from highlands to lowlands and floodplains through networks of streams, active channels or dry gullies (also called

* Corresponding author at: ONERA, DOTA, Université de Toulouse, F-31055 Toulouse, France.
E-mail addresses: arnaud.cerbelaud@onera.fr, arnaud.cerbelaud@cnes.fr (A. Cerbelaud).

https://doi.org/10.1016/j.isprsjprs.2021.10.013
Received 30 July 2021; Received in revised form 20 September 2021; Accepted 23 October 2021
Available online 31 October 2021

ephemeral rivers; Cerdà et al., 2021). Rain transport can be set off either when maximum soil moisture content is exceeded or because rainfall rate overcomes infiltration capacity (known as Horton overland flow; Horton, 1933). It can occur both in gentle bare slopes or steep vegetated areas. In regions where vegetation cover is relatively poor with unstable, barren surfaces or where terrain is rather steep, water flow can quickly reach great velocities and extensively erode soils and bedrocks (Horton, 1945). Rainwater-related damages can thus appear under many forms and on multiple surfaces.

With the growing availability of high revisit frequency and high spatial resolution satellite data at global scale in recent years, flood-related deteriorations can now be quickly and closely assessed. As most human communities worldwide are settled in direct proximity to large rivers, the most substantial damages with dramatic socio-economic consequences are usually observed around major waterways. Therefore, the greater part of operational and research endeavors has focused on detecting, assessing and monitoring the spatial and temporal extents of stream overflows (Sheng et al., 2001; Amarnath et al., 2012). To this end, change detection methods based on satellite remote sensing acquired at different dates, from optical and radar sensors, have been thoroughly explored for decades (Rahman and Di, 2017). With climate change likely leading to an increasing number of flood-related disasters around the world (Kharin et al., 2007; Wang et al., 2017), countless methods have been described to efficiently discriminate flooded and flood-prone areas from spaceborne imagery, most of them through direct identification of water bodies. Some have been based on optical instruments like MODIS (Brakenridge and Anderson, 2006; Amarnath et al., 2012), Landsat (Yamagata and Akiyama, 1988; Swain et al., 2020) Kompsat-2 (Byun et al., 2015) or more recently Sentinel-2 (Pulvirenti et al., 2020; Goffi et al., 2020). But the vast majority of them have relied on Synthetic Aperture Radar (SAR) products from C-band instruments like ERS-1/2 (Nico et al., 2000), ENVISAT (Matgen et al., 2011), RADARSAT 1 and 2 (Hostache et al., 2007; Matgen et al., 2011), and lately Sentinel-1 (Twele et al., 2016; Uddin et al., 2019; Rambour et al., 2020; Liang and Liu, 2020; Singha et al., 2020), as well as X-band instruments like TerraSAR-X and TanDEM-X (Martinis et al., 2015; Li et al., 2019). Tavus et al. (2021), Kocaman et al. (2020) and DeVries et al. (2020) used both radar (Sentinel-1) and optical (Sentinel-2, Landsat for the latter study) data to identify inundated areas and rapidly monitor flood events. However, most of these approaches were designed to reveal the presence of ponded water and thus required on-time post event acquisition of flooded areas, even though some of them proposed to partly circumvent this timing issue by using SAR interferometric coherence to detect actual post flood damages (Nico et al., 2000; Plank, 2014, also dealing with earthquakes and other natural disasters).

A significant amount of storm-related disturbances, especially those caused far from active streams by intense rainwater runoff, appear during short, hardly observable time periods, potentially anywhere, and cannot be pinpointed using water-based identification methods. All in all, comprehensive detection of such degradations has yet been somewhat disregarded by the scientific community. Some authors have developed change detection techniques to fully detect areas affected by flood and erosion from a heavy rainfall. Nonetheless, most of them used very distant images (one year apart or more) and with coarse spatial resolution (30 m of Landsat TM; Dhakal et al., 2002), or with higher resolution but once again strictly limited to overflowing (4 m with Kompsat-2; Byun et al., 2015). In addition, these methods were not designed to be easily replicable to other regions and at any time of the year. Mainly relying on multitemporal analysis, multiple associated topics in geosciences have also been investigated for years in the remote sensing community such as the formation of gullies due to rainwater transport (Fadul et al., 1999), the mapping of soil erosion (Dubucq, 1986; Dwivedi et al., 1997; Begueria, 2006; Sepuru and Dube, 2018), the assessment of landslide extents (Danneels et al., 2007; Mwaniki et al., 2015; Heleno et al., 2016) or agricultural losses and crop yields (Pantaleoni et al., 2007; Jiao et al., 2014). In recent years, Plekhov and Levine (2018) used high spatial (3 m) and temporal (daily on a planetary scale) resolution products from the PlanetScope constellation to detect damages to archaeological sites induced by surface runoff after extreme weather events. Simply from visual inspection of NDVI (Normalized Difference Vegetation Index) change images, they concluded that high temporal resolution satellite systems could contribute to better calibrated soil erosion models and help mitigate damages to cultural sites. Beyond the well-established pixel-oriented methods, object-oriented change detection (OOCD) approaches have recently become quite popular in land cover change mapping (Robertson and King, 2011), for example for landslides classification (Huang et al., 2018), in some cases paving the way for better performances.

Very high resolution optical products (VHR, characterized by a sub metric spatial resolution), mostly available from commercial missions such as IKONOS, Quickbird, WorldView, and more recently the French *Pléiades* satellites, have progressively emerged for scientific use. Naturally, they now constitute key elements to detect, assess and monitor natural disasters such as floods, cyclones and earthquakes (see Pléiades Days 2014 journal, RFPT n°209). With 0.5 m spatial resolution and advanced agility due to its large roll capacity, French dual satellites *Pléiades* allow precise and fast (within a day or two) detection of damaged areas following natural disasters. For floods, the presence of water surfaces was easily revealed using simple thresholding schemes based on the four radiometric bands (visible and near infrared), while identification of residual marks such as mudslides was also performed (Yésou et al., 2015a, 2015b). However, in most studies, post flood footprints were mostly tracked down manually on a case-by-case basis, and once again within the direct proximity of overflowing streams. Huber et al. (2013) revealed the complementarity of shortwave infrared (SWIR, with SPOT 5) and VHR data (with *Pléiades*) for flood assessment. They found SWIR bands to be useful for flood detection even during recession in post storm days while VHR images allowed for fine photo-interpretation capacity to detect mud traces and assess global impacts. Even though they mentioned that SWIR was useless to detect mudslides (minerals bear similar signatures), they took advantage of NDVI temporal variations to underline changes in texture, potentially pointing to muddy areas. In other research, Chen et al. (2015) produced high resolution digital elevation models (DEMs) obtained from stereo pairs of *Pléiades* images to simulate the fine structure of river networks and landscape morphology, which could also be helpful in assessing flood damages. However, because VHR satellites do not provide open-source continuous imagery of the entire globe (due to acquisition costs and data volumes), production of change images and simple automation of such processes appears hardly achievable. In addition, optical spaceborne products require on-time clear sky conditions and thus bear inherent limitations.

Aside from direct water identification for flood assessment, a wide range of researchers have investigated the potential of SAR products to retrieve soil moisture contents in weakly vegetated soils (Baghdadi and Zribi, 2016). Zribi et al. (2007) laid out implications of such methodologies to study hydro-meteorological feedbacks between the land surface and lower atmosphere while Baghdadi et al. (2008) underlined their utility for hydrological and erosion modelling. Methods based on both Sentinel-1 (S1) to retrieve soil moisture estimates and Sentinel-2 (S2) to account for vegetation effects have already been investigated (Gao et al., 2017). Bousbih et al. (2017) confirmed that S1 C-band VV and VH polarization signals were sensitive to variations in soil moisture, using NDVI filters from Landsat images and drawing results from *in situ* measurements. Other works have performed physical and empirical backscattering model inversions to retrieve bare soil surface parameters from ERS data (Wagner et al., 1999) and more recently using machine learning techniques from S1 (Mirsoleimani et al., 2019) or RADARSAT-2 (Santi et al., 2019) data. Application to the detection of storm-related damages here deserves to be evaluated. Indeed, should intense rainwater runoff be induced by saturation of soil water content, higher increase in soil moisture could be expected in affected areas compared to

undamaged ones. This should in turn be quantifiable on relatively bare grounds by measuring temporal changes in SAR backscattered signals.

Every year in France, around 3/4 of natural disaster claims are flood-related. However, river overflowing is suspected to be responsible for only half of them (Breil et al., 2016). Due to its ephemeral nature and potential to materialize anywhere in a given region, intense overland rainwater flow is very difficult to witness and monitor *per se*. Nevertheless, its numerous consequences in the form of erosion, mudslides, landslides, uprooting and other kinds of soil degradation are generally characteristic and durable, although damaged infrastructures such as roads are often rapidly restored. This study entirely relies on the assumption that these footprints (deterioration of plant cover, eroded bedrock, mud deposit) can be traced back to specific signatures through spectral variations in time inside homogeneously reacting land areas. Cerbelaud et al. (2020, 2021) outlined the potential of a combined use of VHR optical imagery from *Pléiades,* high revisit frequency multispectral images from S2 and adequate territorial subdivision (plot-based approach using the official land cadastre) to automatically detect different types of damages resulting from extreme hydro-meteorological episodes over large regions, including at any distance from waterways. With a change image produced from two S2 acquisitions made 10 days before and after a storm, they reached up to 90% overall accuracy in discriminating damaged plots using intra-plot statistics such as pixels mean and variance of the relative difference of adequate spectral indices.

Still, detecting the different spatial patterns in optical and radar change images induced by floods requires controlling for seasonal transformations and anthropogenic activities as well as for the potentially unique and distinctive reactions of each land cover to intense precipitations between the studied images. Ensuing the works of Cerbelaud et al. (2020, 2021), this issue was addressed here by developing a change detection method based on the association of multiple products and tools, essentially:

i. the use of both optical and SAR multitemporal open-source data from Sentinel-1 and Sentinel-2 satellites with 10 m spatial resolution (20 m for SWIR);
ii. a contextual plot-based approach so as to highlight heterogeneous changes within piecewise constant land cover areas;
iii. the development of an automatic detection scheme based on supervised classification relying on the combined search for statistical patterns in spectral, spatial and temporal variations among damaged plots;
iv. a simple land use inter-class demeaning pre-processing designed to minimize false positives by clearing off part of the various impacts of seasonal transformations and local anthropogenic activities in the change images as well as to improve event and site replicability;

Three independent extreme hydro-meteorological events were examined in this paper. It allowed to showcase this work's strength, i.e. repeatability, by using a uniquely trained classifier from the first event to map damages over the two other events which occurred at different seasons or over contrasted terrain. Furthermore, a multitemporal analysis was carried out for robustness checks in order to test the stability of the method in hypothetical conditions of persistent cloud cover. Contribution of SAR signal to maintain good classification capability in combination with more distant optical images was also tested. Reliability of the methodology stemmed from deriving classification capability from large samples of certified ground truths along with validation data based on photo-interpretation of VHR post event images from *Pléiades* satellites and IGN (French National Institute of Geographic and Forest Information) *orthophotos* with sub metric resolution. This study goes beyond the traditional investigation of case studies and demonstrates not only the performance but the repeatability potential of a change detection method to expose numerous types of extreme rainfall-related hazards. It aims in particular at exhaustively identifying deteriorations occurring far from the main hydrographic network, which has been scarcely studied until now. Should spatially accurate rainfall products be available, this original plot-based approach will contribute to improving the understanding of overland flow generation mechanisms in hydrological models.

After presenting the study regions, the materials and detailing the approach in Section 2, results are interpreted and analysed on three distinct events in Section 3. Section 4 further discusses these results and conclusive statements are eventually provided in the last section.

2. Materials and methods

2.1. Study area, territorial subdivision and land use categories

This study focuses on three extreme Mediterranean events that led to flash-flooding characterized by river overflowing and intense rainwater runoff in contrasted manners in the years 2018 and 2020. These events all occurred in the South of France with high intensity precipitations and will be hereafter referenced as:

i. *Aude 1:* a significant storm in the Aude department on October 15, 2018, with close to 300 mm of rainfall measured around the city of Carcassonne within a 24 h-period, and up to 250 mm locally in only 6 h (Lebouc et al., 2019);
ii. *Aude 2:* a weaker event in the Aude department on May 11, 2020, with 175 mm of rainfall measured in 48 h around the towns of Martys and Montolieu (Source: Météo-France);
iii. *Alpes-Mar.*: the "*Alex*" storm in the Alpes-Maritimes department on October 2 and 3, 2020, with around 500 mm of rainfall estimated at Saint-Martin-Vésubie in 24 h (corresponding to return periods between 500 and 5000 years), and up to 90 mm in only one hour at Coursegoules rain station, which caused the formation of countless landslides and gullies (see Carrega and Michelot, 2021).

For this work, the first two regions of interest were selected over roughly 1 150 km^2 for *Aude 1* and 546 km^2 for *Aude 2* in the Fresquel, Orbiel and Aude watersheds. The study area for *Alpes-Mar* covered the Tinée, Vésubie and Roya valleys, representing 1 120 km^2 of steep mountainous woodlands. Regions were chosen based on the lists of cities declared in a "natural disaster" state by inter-ministerial order as well as on the availability of VHR images. A map describing the precise location of all three study sites is provided in Fig. 1.

The *Aude 1* and *Alpes-Mar* events were covered by activation of the Copernicus Emergency Management Service (EMS) under the activation numbers EMSR324 and EMSR467. Grading maps delivered within a week after the events clearly showed delimitations of overflowing streams and mud traces nearby, especially around Trèbes and Villalier for *Aude 1*, but very scarcely inspected larger and more distant areas for traces of overland flow.

In order to operate at a plot scale, the Aude and Alpes-Maritimes official department land cadastre datasets were retrieved under QGIS 3.18 to obtain the most natural territorial subdivision with piecewise constant land use (grey box in Fig. 2). The areas of interest comprised around 200 000 plots under the 2018 version of the land cadastre for *Aude 1*, 100 000 plots for *Aude 2* and 140 000 plots for *Alpes-Mar*. Plots average areas were respectively of 0.5, 0.5 and 0.7 ha with high standard deviations of 1.7, 1.4 and 5.3 ha due to the disparities between urban, rural and remote territories. The OSO French land cover product (Inglada, 2018) available at a 10 m spatial resolution was used to determine the main land use (LU) category within each plot (dark green box in Fig. 2). According to the OSO 2018 raster, most of the study zones were covered up with grasslands (30% of pixels for *Aude 1*, 30% of pixels for *Aude 2* and 31% of pixels for *Alpes-Mar.*), vineyards (24%, 13% and 0%), forests (20%, 21% and 65%), built-up (14%, 18% and 1%) and

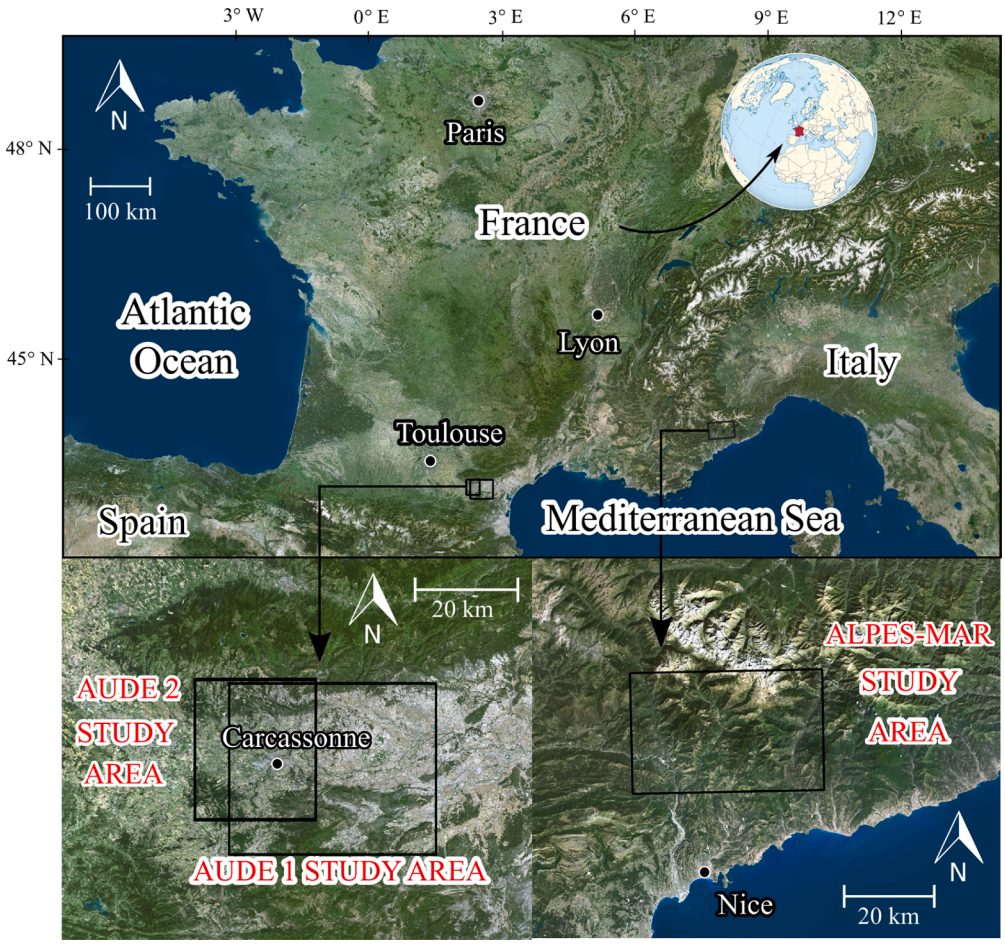

Fig. 1. Study areas in Aude and Alpes-Maritimes departments, France (IGN airborne *orthophotos*, 2017).

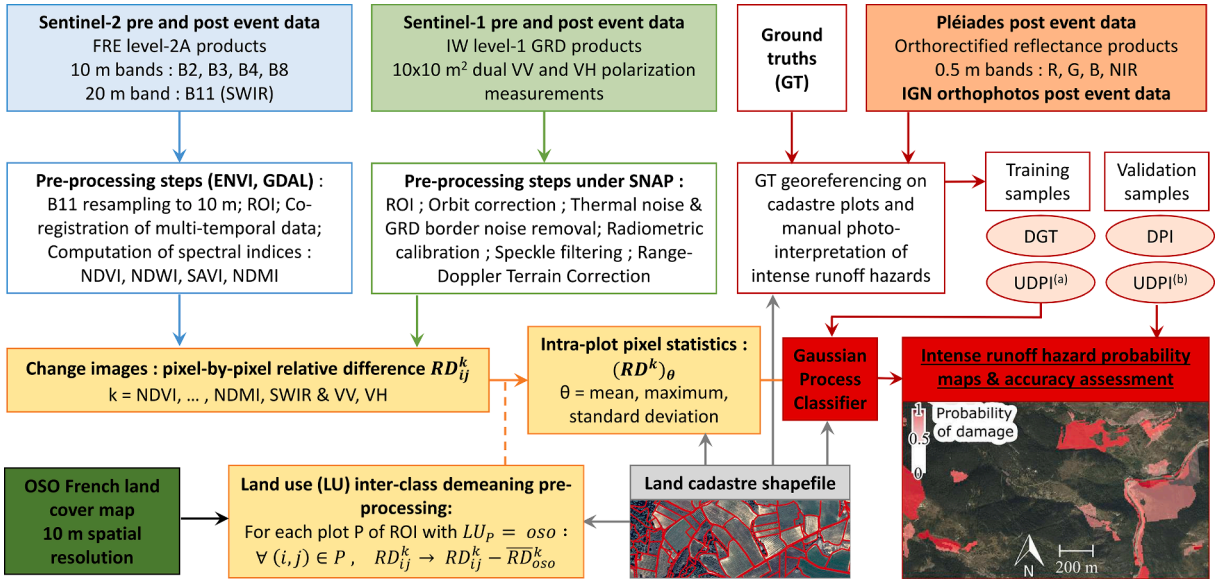

Fig. 2. Methodological workflow of the study.

other types of crops (cereals, protein crops, sunflower etc.; 12%, 18% and 0%).

2.2. Satellite multispectral optical imagery and synthetic aperture radar products

Three complementary types of satellite products were acquired for this work (Table 1). First, the earliest post event very high resolution

Table 1
Acquisition dates and imaging capabilities of *Pléiades*, IGN airborne, Sentinel-2 (non-exhaustive) optical instruments and Sentinel-1 radar instrument.

Satellite product	Acquisition dates Event X : Date t			Wavelength range (nm)	Spatial resolution
	***Aude 1*: Oct. 15, 2018**	***Aude 2*: May 11, 2020**	***Alpes-Mar*: Oct. 3, 2020**		
***Pléiades* - Optical**	*Post* event: 2018/11/03 2019/02/22	*Post* event: 2020/05/22	*Post* event: *2020/10/05* *2020/10/13*	Panchromatic 480–820 Blue (B0) 450–530 Green (B1) 510–590 Red (B2) 620–700 NIR (B3) 775–915	0.7 m (panchromatic) 2.8 m (multispectral) Resampled to 0.5 m (all bands)
IGN *orthophotos* - Optical			*Post* event: *Multiple tiles starting 2020/10/05*	Visible (blue, green and red)	~ 0.15 m
Sentinel-2 (S2) - Optical	*Pre* event: 2018/08/16 2018/09/25 2018/10/05 *Post* event: 2018/10/25	*Pre* event: 2020/03/18 2020/04/10 2020/05/07 *Post* event: 2020/05/20	*Pre* event: 2020/08/22 2020/09/13 2020/09/28 *Post* event: 2020/10/08	Blue (B2) 460–525 Green (B3) 542–578 Red (B4) 650–680 NIR (B8) 780–886 SWIR (B11) 1565–1660	10 m for bands B2, B3, B4 and B8 20 m for band B11
Sentinel-1 (S1) - SAR (IW-GRD)	*Pre* event: 2018/10/11 *Post* event: 2018/10/17	*Pre* event: 2020/05/09 *Post* event: 2020/05/14	*Pre* event: 2020/09/26 *Post* event: 2020/10/08	C-band 5.55 cm (5.405 GHz central frequency)	10×10 m^2 for GRD product

(VHR) *Pléiades* images (orthorectified reflectance products corrected for atmospheric effects) were used to confirm and/or to visually identify traces of overflowing and rainwater runoff on agricultural lands, grasslands, roads and other diverse works (orange box in Fig. 2). With 6.5 m location accuracy, four spectral bands in the visible and near-infrared (NIR) and a 0.5 m multispectral resampled spatial resolution, this product was a very valuable tool to differentiate damaged from non-affected areas by manual photo-interpretation. Different types of damages were thus identifiable: landslides and mudslides, gullies, erosion, sediment deposit and vegetation uprooting. For the *Alpes-Mar* event, airborne *orthophotos* were acquired by IGN with a 0.15 m spatial resolution and a geometric accuracy lower than 1 m (orange box in Fig. 2). These images taken shortly after the "*Alex*" storm were even more profitable for precise photo-interpretation purposes, although lacking a NIR channel. *Pléiades* and IGN *orthophotos* were not co-registered as they were georeferenced sufficiently well to be used for manual photo-interpretation.

Secondly, multiple images from two S2 tiles were acquired at different dates and co-registered to allow for accurate generation of change images: T31TDH for *Aude 1* and *Aude 2* and T32TLP for *Alpes-Mar*. These ready-to-use products consisted in Flat Reflectance (FRE) data with level-2A treatment, corrected for atmospheric effects and with cloud and shadow masks, either from Sentinel-2A or 2B satellites (blue box in Fig. 2). Co-registration was performed using ENVI with post event images as reference images. Each resulting pair of S2 acquisitions presented values of average sum-of-squared intensity differences (SSD) lower than 0.002 on all three study events. Along with a 12 m location accuracy and a medium spatial resolution of 10 m for visible and NIR bands, S2 optical data was the key asset to this work through its great revisit frequency (around 5 days) allowing to closely monitor spectral variations before and after each event (Table 1). Following a 10 m resampling using GDAL library, the B11 SWIR band was also used in this work as a promising candidate for detection of post-flood traces (Yésou et al., 2003). Several pre event images were obtained in order to test the stability of the method in hypothetical conditions of persistent cloud cover.

Eventually, in order to evaluate SAR potential to detect potentially impacted areas, the closest Interferometric Wide Swath (IW) level-1 Ground Range Detected (GRD) S1 products were also retrieved for all three events (light green box in Fig. 2). They consisted in 10×10 m^2 spatial resolution, dual VV and VH polarization measurements. Contrary to S2, these products were not ready-to-use. Following the workflow of Filipponi (2019) and using SNAP software and its Sentinel-1 toolbox (SNAP v7.0, 2018), several pre-processing operations were performed on the S1 raw data so that change images could be generated and stacked to S2 change images for adequate computations:

- Subset of the region of interest (ROI);
- Orbit correction (ascending or descending);
- Thermal noise and GRD border noise removal;
- Radiometric calibration (sigma for *Aude 1* and *Aude 2* and beta for *Alpes-Mar*) to convert the digital values of the raw images into backscattering coefficients;
- Speckle filtering with a Lee Sigma filter (Lee and Pottier, 2009);
- Range-Doppler Terrain Correction with the RGE ALTI ® DEM from IGN at 5 m spatial resolution.

A beta radiometric calibration was used for the *Alpes-Mar* event compared to *Aude* study sites as it is advised on high relief terrains. Finally, a logarithmic transformation was applied to backscattering coefficients to convert them into dB values. All products were used (and projected to if necessary) in the native reference coordinate system of Sentinel images, World Geodetic System (WGS) 84, either Universal Transverse Mercator (UTM) zone 31 N for *Aude 1* and *Aude 2* or UTM zone 32 N for *Alpes-Mar*.

2.3. Selection of ground truths and photo-interpreted plots

Following the preliminary work of Cerbelaud et al. (2021) on the *Aude 1* event, two additional validation samples were put together (white box outlined in red in Fig. 2) so as to evaluate replicability potential of the change detection method at different seasons (*Aude 2*) and on areas with contrasted land use and topography (*Alpes-Mar*). Table 2 describes (i) the ground truths sources and sample selection methods; (ii) the image products and dates used for photo-interpretation and (iii) the classes contents. Tagged observations from all three events can be seen in Fig. 3.

For the *Aude 1* catastrophe of October 15, 2018, the same dataset of geo-referenced plots that was assembled by Cerbelaud et al. (2021) on the department land cadastre was used. Based on around 900 claims for agricultural disaster that were registered and certified by the local authorities (Aude's *Direction Départementale des Territoires et de la Mer*, DDTM 11) following the event, 310 damaged plots were singled out after visual inspection of the closest post event *Pléiades* image from

Table 2
Description of training and validation samples used for all study sites.

	***Aude 1*: Oct. 15, 2018**	***Aude 2*: May 11, 2020**	***Alpes-Mar*: Oct. 3, 2020**
Ground truths source	Around 900 agricultural disaster claims obtained from local authorities (DDTM 11) with around 1 000 locations geo-referenced on the land cadastre	Closed-off road segments obtained from local authorities (DDTM 11). Damages were searched for in the surrounding areas and tagged on the land cadastre	Field campaign in February 2021 for the *Hymex* National Program: observations from Sospel to the Roya and Vésubie valleys. Road collapses and covered in mud, landslides and rockslides were GPS-located on the land cadastre
Post event VHR image for photo-interpretation	*Pléiades* Nov. 3, 2018 (0.5 m)	*Pléiades* May 22, 2020 (0.5 m)	IGN *orthophotos* Oct. 5, 2020 (0.15 m) - *Pléiades* Oct. 5, 2020 (0.5 m)
Number of plots in resulting data samples	Training: 310 $DGT^{(1)}$ Validation: 362 $DPI^{(1)}$ Training & validation: 480 $UDPI^{(1)}$	Validation: 184 $DPI^{(2)}$ 497 $UDPI^{(2)}$	Validation: 435 $DPI^{(3)}$ 571 $UDPI^{(3)}$

November 3, 2018, to form the *Damaged Ground Truths* training sample, named hereafter $DGT^{(1)}$. The approval strategy of these plots out of all agricultural disaster claims was specified in Cerbelaud et al. (2021). 362 additional damaged but yet unclaimed plots (*Damaged Photo-Interpreted* - $DPI^{(1)}$ - sample) were also hand-picked independently using the same VHR image in the surrounding areas for validation purposes. Finally, 480 unaffected lands (*Undamaged Photo-Interpreted* - $UDPI^{(1)}$ - sample) were selected with a similar methodology close-by as well as further away from the damaged areas for the control group.

For *Aude 2*, the $DPI^{(2)}$ damaged validation sample was constituted using information regarding the different road segments that were closed-off during the event (source DDTM 11). However, because the precise location of flooded and/or damaged road sections were not detailed in the available files, the *Pléiades* image from May 22, 2020, was closely inspected to identify 184 damaged plots in the direct vicinity of the closed roads. An undamaged $UDPI^{(2)}$ sample of 497 plots, as representative as possible of the distribution of land use types in the area, was then compiled from different locations to make sure that a limited number of false positives were flagged by the classification algorithm.

In the context of the French national *Hymex* program that seeks to improve understanding and modelling of hydro-meteorological hazards in the Mediterranean region, a field campaign was carried out in February 2021 from Sospel to the Roya and Vésubie valleys. There, terrain specificities were assessed and affected areas were located. GPS coordinates for mountain roads that had been covered in mud or that had collapsed as well as deteriorations (landslides, gullies, rockslides) for which intense rainwater runoff was undeniably accountable were recorded. Because the observation campaign took place around five months after the events, small disturbances, especially near urban areas, had been mostly cleaned up. However, due to the difficulty in accessing remote areas, a significant amount of deteriorations was still visible on the mountain slopes down to valleys, with road works still underway in numerous places. Following this campaign, 435 damaged lands $DPI^{(3)}$ were finally tagged on the Alpes-Maritimes land cadastre using the VHR (0.15 m) IGN *orthophotos* around the visited areas as well as in the Tinée valley. Lastly, a $UDPI^{(3)}$ unaffected validation sample of 571 plots was assembled to complete the overall *Alpes-Mar* dataset with the same methodology.

Sample images for all classes and study areas can be seen in Fig. 4. In order to make sure that the resulting datasets were representative of each study area and that DPI ($DGT^{(1)}$ for *Aude 1*) and UDPI classes were somewhat comparable, the main characteristics of each class were estimated (Table 3). In addition, the distribution of plots' major land use (OSO), overall and by class, excluding the built-up category, is shown in Fig. 5. Logically, vineyards were over-represented in the *Aude 1* and *Aude 2* study regions, along with sunflowers and cereal crops. For these events, damaged plots tended to be much more located in agricultural lands, since they were more easily recognizable, than in woodlands and grasslands. UDPI and DPI classes showed slightly dissimilar land cover distributions that could induce small statistical biases in spectral signatures. This concern is partially addressed in Section 2.5. For the *Alpes-Mar* event, only two land use types dominated (grasslands and forests), with a similar distribution overall and between the two classes.

Mean slope was derived for all study regions from the RGE ALTI ® DEM (5 m spatial resolution) from IGN. Overall, the complete tagged area added up to around 26 km^2 (i.e. 2.3% of the total region) for the *Aude 1* study site, 12.3 km^2 (2.3%) for *Aude 2* and 7.3 km^2 (0.7%) for *Alpes-Mar*.

2.4. Supervised classification change detection method based on plot-specific spectral indicators

Ensuing the works of Cerbelaud et al. (2020, 2021), this study relied on information derived from soil and vegetation-specific spectral indices based on the visible and NIR 10 m bands of S2 images. Building on from the conclusions of these two previous studies, three suitable indices were kept here: NDVI, NDWI for Normalized Difference Water Index (McFeeters, 1996) and SAVI for Soil Adjusted Vegetation Index (Qiu et al., 2017; see Table 2 from Cerbelaud et al. (2020) for details). The B11 SWIR band and the NDMI for Normalized Difference Moisture Index (Gao, 1996) were also used as indicators of vegetation water content. Physics-wise, this study's core assumption remained that intense overland water flow can be traced back to erosion marks, mudslides, various deposits and uprooting through measurable spectral variations in time and space. This study also aimed at bringing new insights through the investigation of SAR data (VV and VH polarizations) contribution to detect recently impacted areas as a proxy in low NDVI areas.

Therefore, new images, called change images, were produced for all spectral indices k from S1 and S2 products (yellow box in Fig. 2) by computing the pixel-by-pixel relative difference (RD) between the pre (t_1) and post (t_2) event images (cloud-free for optical data), called change pixels and written RD^k. Particular attention was thus paid to the accuracy in the co-registration of Sentinel tiles.

$$\forall\, k \in [\mathrm{NDVI}, \mathrm{NDWI}, \mathrm{SAVI}, \mathrm{B11}, \mathrm{NDMI}, \mathrm{VV}, \mathrm{VH}]:$$
$$\forall\, (i,j) \in S, \qquad RD^k_{ij} = \frac{BV^k_{ij}(t_1) - BV^k_{ij}(t_2)}{BV^k_{ij}(t_1) + BV^k_{ij}(t_2)} \tag{1}$$

where S designates the overall image extent and $BV^k_{ij}(t_{1(2)})$ the brightness value of pixel (i,j) for index k at pre (post) event date t_1 (t_2).

In order to highlight the presence of spatial heterogeneities as well as singular spectral variations within damaged plots, plot-based pixel statistics θ were estimated for all three events on each change image to produce plot-specific vectors of characteristics $(RD^k)_\theta$ (yellow box in Fig. 2, see examples on Fig. 6). The most relevant statistics found in Cerbelaud et al. (2020, 2021) were computed: mean, maximum (max) and standard deviation (std). The mean and maximum metrics were selected to relay positive values of RD^k so as to indicate decreases in the NDVI and SAVI indices (they are mostly positive) and increases in the NDWI as well as in the SAR indices (they are rather negative) following the events. For all three optical indices, such RD^k values implied a deterioration in vegetation cover following intense rainwater overland flow. For VV and VH radar signals, they suggested an increase in soil

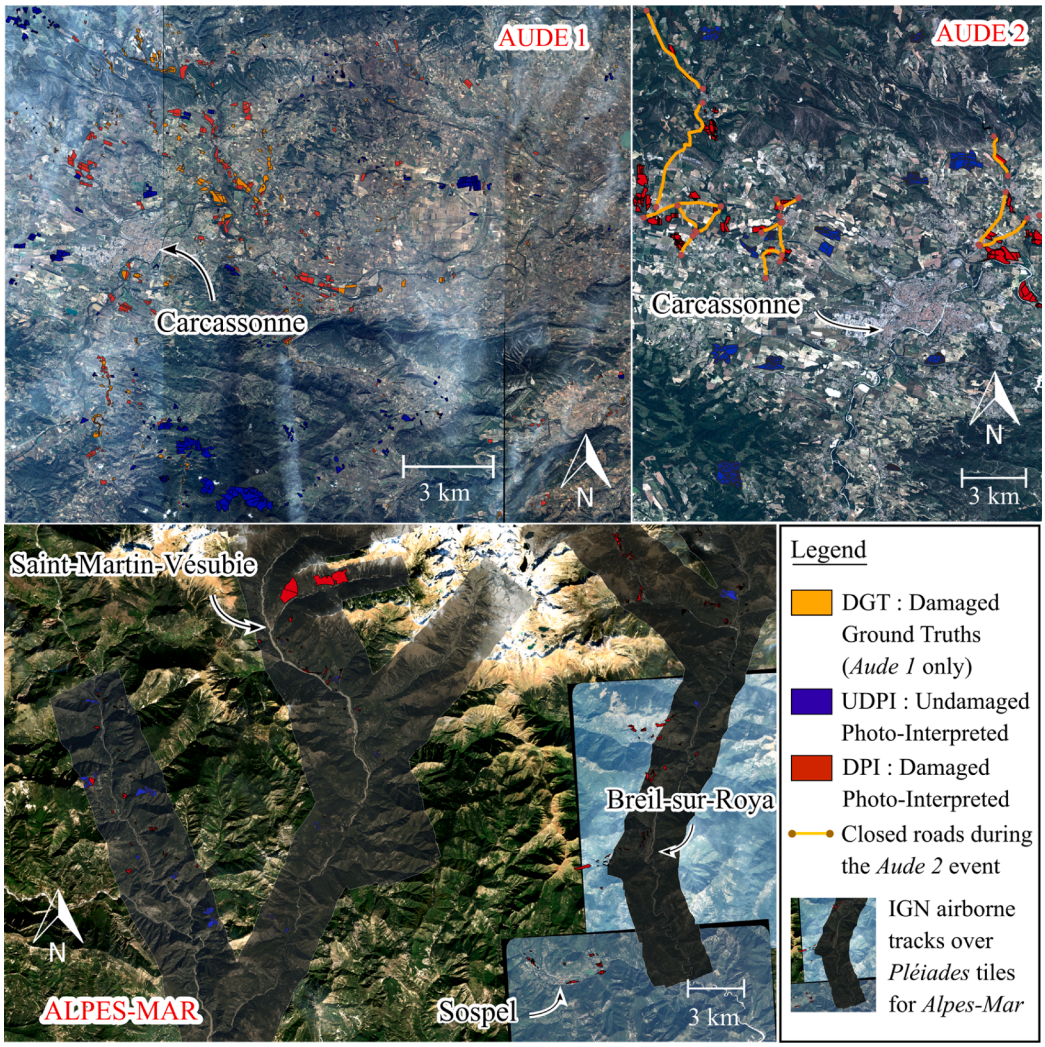

Fig. 3. Identifiable damages and undamaged plots on all study sites. Roads that were closed-off following flood damages for the May 11, 2020, event in *Aude 2* study site were marked with orange lines. Background images are from *Pléiades* images for *Aude 1* and *Aude 2*. Some thin cloud cover can be observed on *Aude 1*. For *Alpes-Mar*, the airborne tracks of the IGN *orthophotos* along with two *Pléiades* tiles were overlaid to the Sentinel-2 closest post event image (Table 1). (For interpretation of the references to color in this figure legend, the reader is referred to the web version of this article.)

moisture and/or roughness (Gao et al., 2017) that could be associated with damage likeliness. Because sensitivity of SAR backscattered coefficients to ground properties has been reported to decrease with increasing vegetation cover growth (Bousbih et al., 2017), a NDVI filter computed on the pre and post event S2 data was applied to S1 change images. Therefore, only changes for pixels with NDVI values lower than 0.25 or 0.5 were considered. Values of RD^k for B11 SWIR band and NDMI index on affected areas were also expected to stand out, yet with less *a priori* assumption on a unique positive or negative pattern depending on the source of identified hazards (Yésou et al., 2003). Due to the distinctive reactions of some land covers to intense precipitations, having the most natural territorial subdivision with piecewise constant land use was crucial in this approach.

With a focus on developing an automatic damage detection method, a unique training sample was put together from the *Aude 1* event, since previous results from Cerbelaud et al. (2021) had confirmed the relevance of the approach on this site. The UDPI$^{(1)}$ undamaged class of 480 plots was thus split in half (yielding two UDPI$^{(1,a)}$ and UDPI$^{(1,b)}$ classes) with a random seed under Python 3 both for training and validation purposes. The learning sample was then assembled from both the ground truths DGT$^{(1)}$ damaged class and the UDPI$^{(1,a)}$ class, adding up to a total of 550 plots on a 11.3 km^2 area. The damaged photo-interpreted DPI$^{(1)}$ class formed the *Aude 1* validation sample along with the other UDPI$^{(1,b)}$ class (602 plots, 14.6 km^2). Validation samples for the two other events were finally directly compiled from their respective DPI and UDPI classes (681 plots, 12.3 km^2 for *Aude 2* and 1 006 plots, 7.3 km^2 for *Alpes-Mar*; see Table 3).

Lastly, plot-based supervised classifications were achieved using a Gaussian process classifier (GPC, red box in Fig. 2) with squared-exponential kernel based on two of the most performing combinations of $(RD^k)_\theta$ indicators found in Cerbelaud et al. (2021) (see their Table 4), complemented or not with SWIR or SAR indicators: $[(RD^{NDVI})_{\text{std}}; (RD^{NDWI})_{\text{max}}]$ and $[(RD^{NDVI})_{\text{std}}; (RD^{SAVI})_{\text{mean}}]$. Gaussian processes for classification are a generalization of the Gaussian probability distribution and a type of non-parametric kernel-based machine learning algorithm. They combine consistent formulations with computational tractability and were chosen in this work mainly because they can give a reliable estimate of their own uncertainty (Rasmussen and Williams, 2006). Performance was measured through overall accuracies and producer accuracies by class, which correspond to the ratio of plots correctly classified within each described class. False alarm rates were also closely monitored to give a representation of the proportion of plots incorrectly identified as affected (DPI) by the GPC (i) among all plots classified as affected (false discoveries) or (ii) among all plots described as undamaged (false positives). GPC results ultimately allowed producing hazard assessment maps with an associated class probability indicating classifier confidence for damage identification.

2.5. Land use inter-class demeaning pre-processing

The damage detection scheme developed in this study relied on discriminatory capacity of plot-based statistics such as mean, maximum

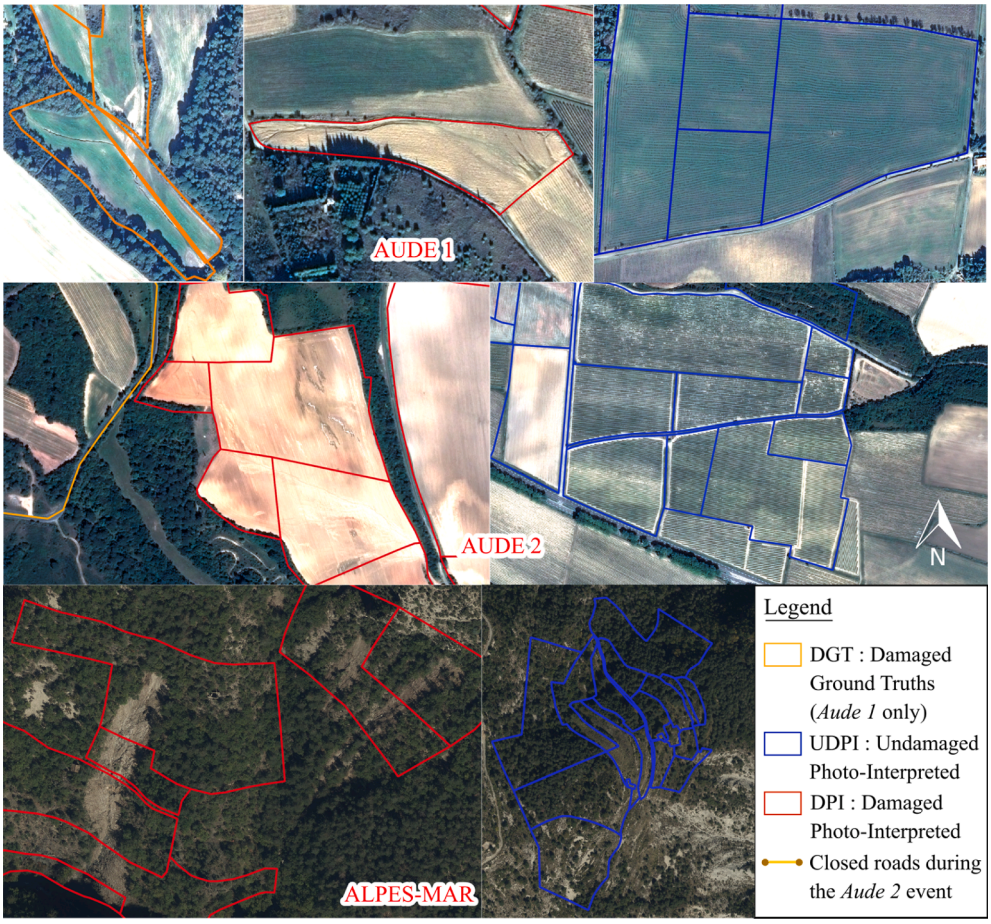

Fig. 4. Sample images from intense runoff hazards and unaffected lands for each class and study area.

Table 3
Characteristics of sample classes in the three study zones.

Sample class	*Aude 1*: Oct. 15, 2018				*Aude 2*: May 11, 2020				*Alpes-Mar*: Oct. 3, 2020			
	Number of plots	Total surface (km^2)	Median plot area (ha)	Mean slope (°)	Number of plots	Total surface (km^2)	Median plot area (ha)	Mean slope (°)	Number of plots	Total surface (km^2)	Median plot area (ha)	Mean slope (°)
UDPI (Undamaged photo-interpreted)	480	11.6	1.27	3.2	497	6.8	0.72	5.6	571	2.6	0.15	24.4
DGT (Damaged ground truths)	310	5.5	0.98	3.1								
DPI (Damaged photo-interpreted)	362	8.8	1.34	2.1	184	5.5	1.10	2.7	435	4.7	0.27	26.5

and variance of change pixels. However, spatially homogeneous changes and irregularities can occur naturally within plots depending on their location, the distribution of their land cover and the ongoing season. Because this classification approach was also designed to be replicable from one event to another, plot statistics of observed changes in spectral signatures for each class (UDPI versus DPI) needed to coincide in terms of both magnitude and distribution for all events. Therefore, the average impact of seasonal transformations and human practices (e.g. bloom in spring, soil moisture states during rainy seasons, fallow and harvest periods) that are usually area, time and land cover-specific needed to be cleared off as much as possible from the change images.

Thus, a land use inter-class demeaning pre-processing consisting in two steps was carried out on all changes images (yellow box in Fig. 2).

Two approaches were considered for the second step. The procedure could be described under the following terms:

1. for a given spectral index k from a given change image S with grid points (m,n), the mean values of all the RD^k_{mn} pixels featuring the same land use type $LU_{mn} = oso$ were computed over the whole study area:

$$\forall\ oso,\ \overline{RD}^k_{oso} = \frac{1}{\sum_{(LU_{mn\in S}=oso)}} \sum_{(LU_{mn\in S}=oso)} RD^k_{mn} \quad (2)$$

2. then

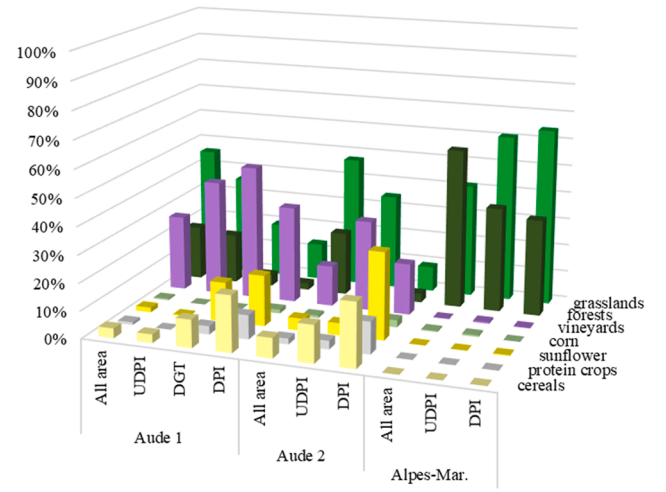

Fig. 5. Land use distribution of plots by class (OSO) in the three study zones.

3. either these mean values $\overline{RD}^{k}_{oso}$ were subtracted to all the change pixels RD^{k}_{ij} of S featuring the corresponding land cover type $LU_{ij} = oso$, regardless of plot subdivision:

$$\forall (i,j) \in S | LU_{ij} = oso, RD^{k}_{ij} \rightarrow RD^{k}_{ij} - \overline{RD}^{k}_{oso} \quad (3)$$

4. either for a given plot P of S with median land use category $LU_P = oso$, these values $\overline{RD}^{k}_{oso}$ were subtracted to all the change pixels RD^{k}_{ij} of P, regardless of their exact land cover type LU_{ij}:

$$\forall P \subset S | LU_P = oso, \forall (i,j) \in P, RD^{k}_{ij} \rightarrow RD^{k}_{ij} - \overline{RD}^{k}_{oso} \quad (4)$$

With images close enough in time (a dozen days or so), a large number of plots presented few to no spectral changes at all. Because the OSO land cover product distribution did not systematically perfectly match the land cadastre subdivision, a significant number of plots presented at least a few pixels representative of an additional land use type. Therefore, the 2.a procedure based on demeaning change pixels by their exact land use type, regardless of plot subdivision, occasionally resulted in artificial modification of plots' inner variability. On the contrary, with plot-specific demeaning relying on median land use type, approach 2.b did not introduce any biases nor it altered plots' variance and was thus preferred.

Expected outcome of this procedure was an increase in the likeliness that change pixels standing out in the resulting pre-processed images originated from singular events. The number of false positives was thus expected to decrease with spectral signatures being less land use-specific. By removing average spectral changes in time that can either be negative or positive depending on the ongoing season (e.g. global NDVI values decrease in autumn and increase in spring), better correspondence between spectral responses of the three studied events was assumed as a consequence.

Since damaged lands' change pixels were also included in the calculation of the demeaning terms (for replicability purposes, they can't be excluded because they aren't supposed to be known *ex ante*), a decrease in the detection accuracy for damaged plots was also anticipated. Finally, in step 1, the demeaning terms could have been calculated in a more sophisticated way using multiyear data. Direct computation on the change images only was preferred here in order to improve easiness and repeatability of the method.

This type of dataset demeaning methodology is mainly derived from time series analysis and country panel data econometrics, where they are commonly used to control for time and country fixed effects, allowing better regression power (Petrova and Westerlund, 2020).

3. Results

3.1. Detection accuracy using Sentinel-2 optical indicators only

The results from classification using the unique training sample from *Aude 1* study site onto the closest S2 change images are displayed in Table 4 for all three events: Oct. 5 to 25 (20 days) for *Aude 1*, May 7 to 20 (13 days) for *Aude 2* and Sept. 28 to Oct. 8 (10 days) for *Alpes-Mar*.

First of all, overall accuracy of at least 88% was reached for one or both combinations of indicators on all study areas. No less than 4 out of 5 damaged plots (DPI) were successfully identified by the classifier. As already disclosed in Cerbelaud et al. (2021), the use as a classification variable of the maximum statistics among plots' change pixels (here NDWI) led to a systematic overestimation of damages with higher rates of false discoveries (1 – DPI user accuracy %) and false positives (1 – UDPI producer accuracy %). Larger false discovery rates were found on the weaker *Aude 2* event, mostly owing to the imbalance between the size of $DPI^{(2)}$ and $UDPI^{(2)}$ classes. The opposite mechanism was at stake for the *Aude 1* event with less $UDPI^{(1,b)}$ plots than $DPI^{(1)}$s. Weaker DPI producer accuracy was obtained on the *Alpes-Mar* event. Multiple rationale can be invoked to justify difficulties in identifying these damages from *Aude 1* spectral signatures. First, intensity and total amount of rainfall was substantially higher during the "*Alex*" storm. Along with contrasted land cover and topography, the episode's brutality (see Carrega and Michelot, 2021) likely induced different spectral responses in terms of magnitude and extent. Finally, compared to Aude, territorial subdivision derived from the Alpes-Maritimes department land cadastre might have been less adequate (lower median and greater disparity in plot size; see Fig. 6 for instance) to allow for a correct detection capacity.

Supervised classification was then applied to all plots within the study areas to produce maps displaying probability of damage classification given by the Gaussian process classifier on hundreds of thousands of registered lands from the cadastre. A close-up example of the output map based on $[(RD^{NDVI})_{std}; (RD^{NDWI})_{max}]$ combination over *Alpes-Mar* study site is shown in Fig. 7. The roads covered in mud and the plots directly impacted by the overflowing of the river can be observed in the city of Tende. An important mudslide reaching over to the North of the city was well captured by the change detection method.

3.2. SAR signal segregation potential with Sentinel-1 data

No attempt at implementing backscattering model inversion to retrieve soil moisture estimates was made in this work. Instead, in order to evaluate whether SAR data was a promising tool to significantly discriminate damaged plots, summary statistics were first simply performed similarly to what was carried out in Cerbelaud et al. (2021) for optical indicators.

S1 change images were consistent with the likeliness that damaged areas should present, on average, higher increase in proxies of soil moisture and/or roughness (Fig. 8). Indeed, a weak differentiation was observed with higher values of signal increase for damaged areas (DGT and DPI), implying higher increase in soil moisture and/or roughness as well. In agreement with SAR literature on soil moisture (Bousbih et al., 2017), this relation was found generally stronger for weakly vegetated areas (NDVI < 0.25 compared to NDVI < 0.5) and for the VV polarization.

The maximum statistics (similar results were obtained with the 90th and 95th percentile, not shown) was found the most relevant for inter-class discrimination (compared to mean or standard deviation, not shown). Average magnitude of maximum SAR change pixels turned out to be larger for the *Aude 2* event, likely due to rainfall being further spread over time compared to the other two episodes, leading to higher water infiltration in soils. Consequently, transferability of *Aude 1* radar signatures to *Aude 2* for cross-classification purposes appeared initially challenging. This issue was dealt with using the pre-processing

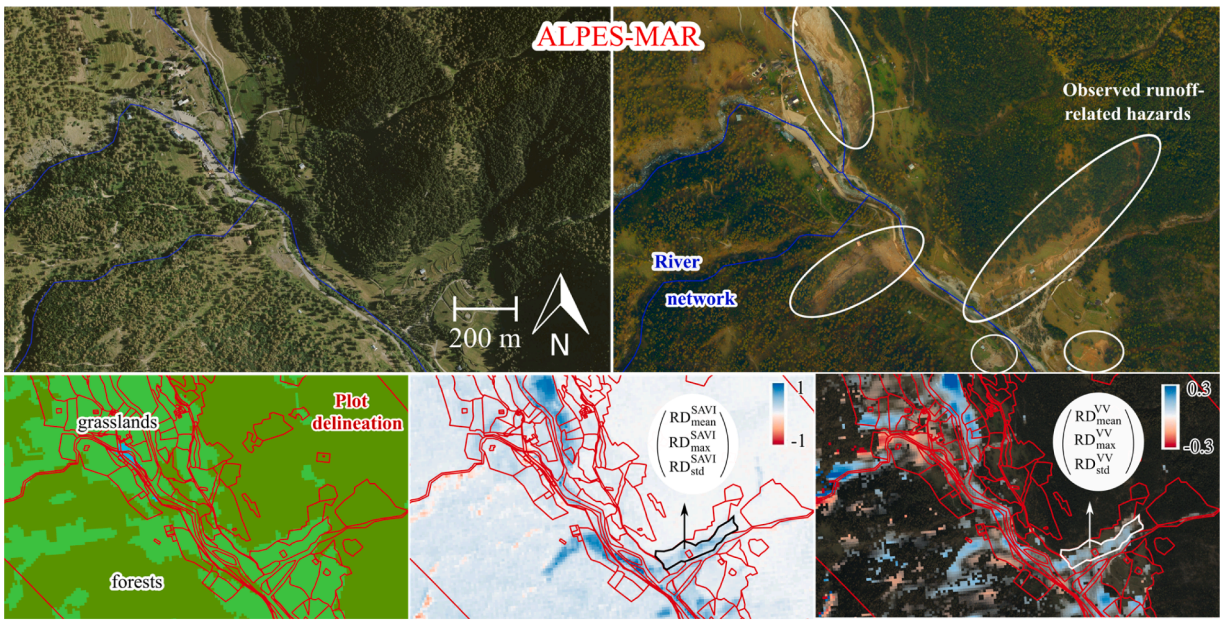

(a) *Alpes-Mar*

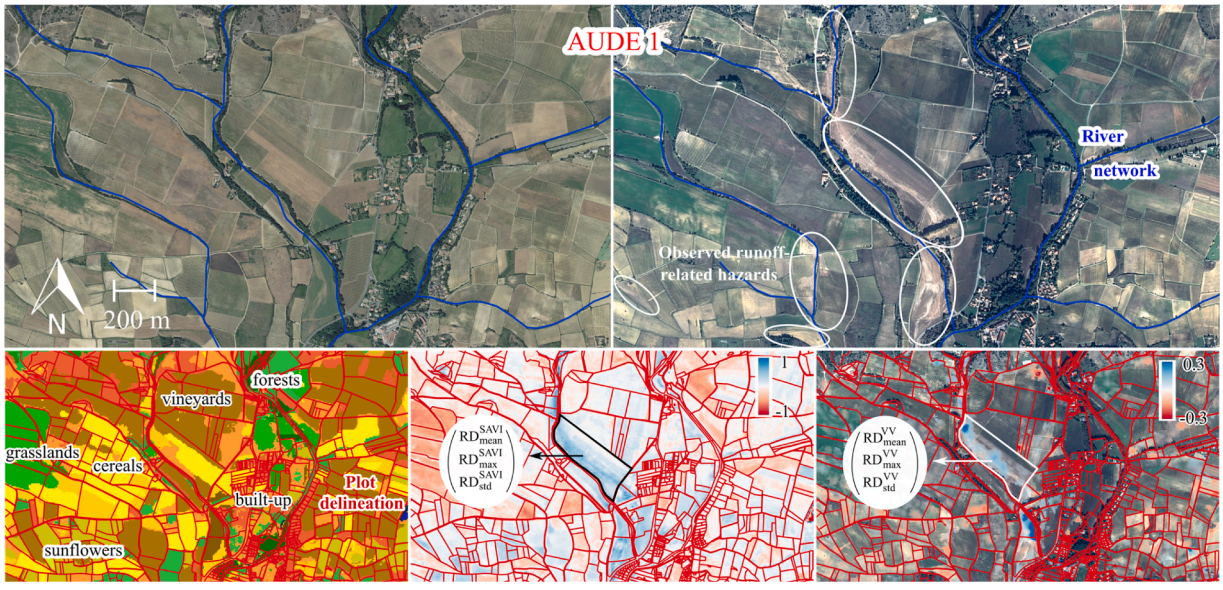

(b) *Aude 1*

Fig. 6. Damages caused by overflowing and intense rainwater runoff following heavy rainfall. Classification strategy based on plot-specific pixel statistics is displayed in the bottom right images. (a) Top left: IGN *orthophotos* 2017 with river network. Top right: IGN *orthophotos* Oct. 5, 2020, post event. Bottom left: OSO land cover on land cadastre. Bottom middle: S2 $\boldsymbol{RD^{SAVI}}$ Sept. 28 - Oct. 8. Bottom right: S1 $\boldsymbol{RD^{VV}}$ where NDVI < 0.25, Sept. 26 - Oct. 8; (b) Top left: IGN *orthophotos* 2017 with river network. Top right: *Pléiades* true colors Nov. 3, 2018, post event. Bottom left: OSO land cover on land cadastre. Bottom middle: S2 $\boldsymbol{RD^{SAVI}}$ Oct. 5–25. Bottom right: S1 $\boldsymbol{RD^{VV}}$ where NDVI < 0.25, Oct. 11–17.

procedure described in 2.5, which is discussed in the next section.

3.3. Cross-site replicability using a land use inter-class demeaning pre-processing

Summary statistics of the different classes among study sites based on the closest raw change images compared to the demeaned ones are displayed in Fig. 9. $(RD^{NDVI})_{std}$ distributions were logically unaffected, since the same constant values were withdrawn from all change pixels of a given plot during the process (Fig. 9a). For this indicator, higher values and a larger variance were observed on *Aude 1* UDPI class compared to the two other events (Fig. 9a). This implied that *Aude 1* change image inherently featured more disparate heterogeneities overall, with important implications on cross detection possibilities that will be discussed in Section 3.5.

$(RD^{NDWI})_{max}$ and $(RD^{SAVI})_{mean}$ distributions (see Fig. 9b and Fig. 9c) from the *Aude 2* and *Alpes-Mar* samples were tilted downwards after demeaning, as opposed to upwards for *Aude 1*. This corrected the fact that RD^k pixels in the *Aude 1* S2 change images were predominantly negative (k = NDVI or SAVI, in response to the extreme weather event; see Fig. 4 of Cerbelaud et al., 2021). With UDPI test distributions being

Table 4
Overall accuracy, producer accuracy by class and false alarm rates from closest change images using optical indicators only.

	550 training plots from ***Aude 1*** - **Oct. 15, 2018**: 240 UDPI[(1,a)] and 310 DGT[(1)]					
	Aude 1 - **Oct. 15, 2018** 602 validation plots: 240 UDPI[(1,b)] and 362 DPI[(1)]		***Aude 2*** - **May 11, 2020** 681 validation plots: 497 UDPI[(2)] and 184 DPI[(2)]		***Alpes-Mar*** - **Oct. 3, 2020** 1006 validation plots: 571 UDPI[(3)] and 435 DPI[(3)]	
Optical indicators $(RD^k)_\theta$ combination	1. NDVI - Std 2. NDWI - Max	1. NDVI - Std 2. SAVI - Mean	1. NDVI - Std 2. NDWI - Max	1. NDVI - Std 2. SAVI - Mean	1.NDVI - Std 2. NDWI - Max	1. NDVI - Std 2. SAVI - Mean
Overall accuracy	89%	89%	91%	89%	88%	83%
UDPI	84%	88%	92%	95%	94%	97%
DPI	92%	89%	86%	71%	80%	65%
False discovery rate	10%	8%	19%	15%	9%	5%
False positive rate	16%	12%	8%	5%	6%	3%

lower than the UDPI training one, better classification scores for unaffected lands was expected after demeaning. Smaller overlaps between UDPI and DPI classes were mostly obtained in the pre-processed RD^{SAVI} and RD^{VV} images for *Aude 1* (see Fig. 9c and Fig. 9d). $(RD^{VV})_{max}$ distribution ranges among all three events turned out to be much more similar once demeaned, specifically for *Aude 2* (albeit rather less for *Alpes-Mar*). As a result, the Gaussian process classifier should be able to better discriminate damaged areas using the demeaned datasets and produce less false positives.

As damaged lands are significantly less numerous than unaffected areas when studying a sufficiently large region, emphasis was placed on achieving highest UDPI accuracies (or equivalently lowest false alarm rates). Classification scores for the two combinations of sole optical indicators as well as complemented by SAR $(RD^{VV})_{max}$ variable (with NDVI < 0.25 filter) are shown in Table 5. The benefits of (i) applying the demeaning pre-processing (when used, it is applied to both training and validation samples) to lower false alarm rates and (ii) using SAR data to improve classification accuracy can be derived from these tables.

First off, the use of pre-processed change images for detection purposes did result in a decrease in the number of plots incorrectly classified as damaged, with lower false discovery and false positive rates, except for the $[(RD^{NDVI})_{std}; (RD^{SAVI})_{mean}]$ combination on *Aude 1*. However, it turned out to be generally at the cost of lower identification capacity for damaged plot samples, mostly leading to slightly lower overall accuracies. This could very well mean that, for some damaged plots featuring

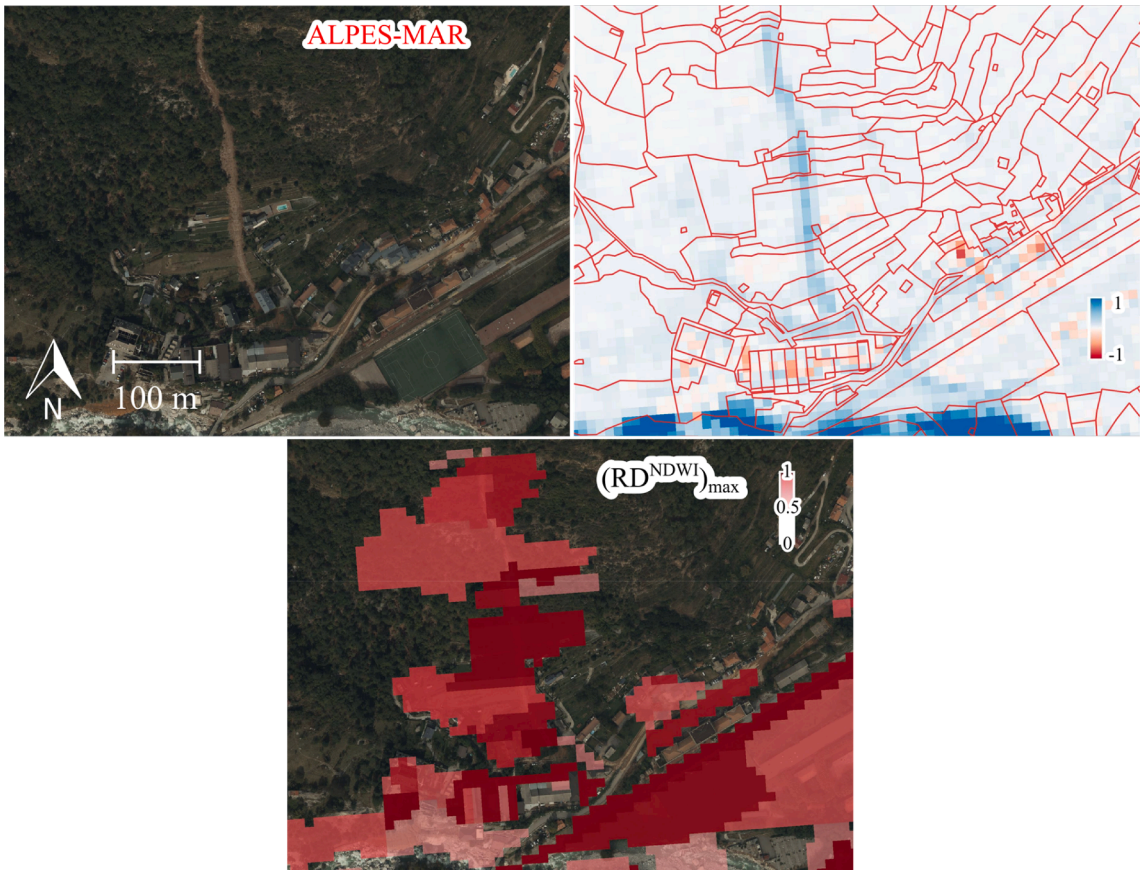

Fig. 7. Mudslide around the city of Tende (06). Top left: IGN *orthophotos* Oct. 5, 2020 post event. Top right: Sentinel-2 $\boldsymbol{RD^{NDVI}}$ Sept. 28 - Oct. 8 over land cadastre. Bottom: Output map displaying the probability of damage classification by Gaussian Process classifier on *Alpes-Mar*, based on $[(RD^{NDVI})_{std}; (RD^{NDWI})_{max}]$ optical combination.

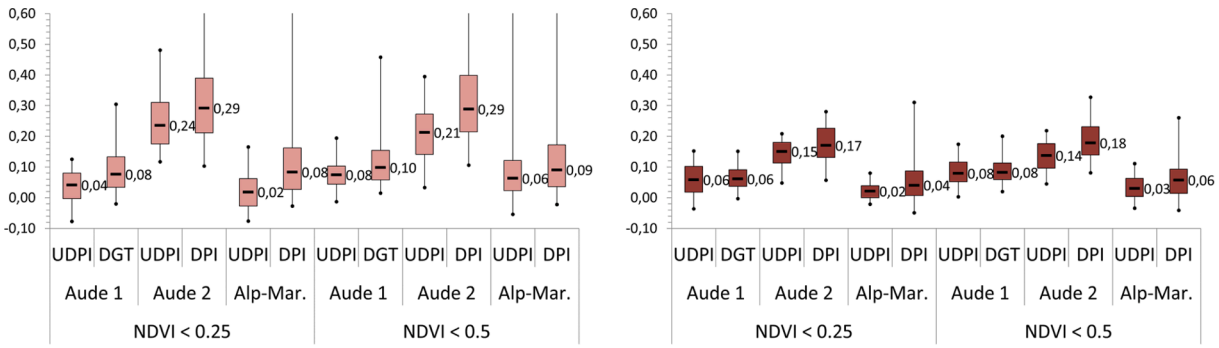

Fig. 8. Boxplot of $(RD^k)_\theta$ distributions depending on NDVI threshold considered for S1 SAR change images. (a) k = VV polarization, θ = maximum; (b) k = VH polarization, θ = maximum.

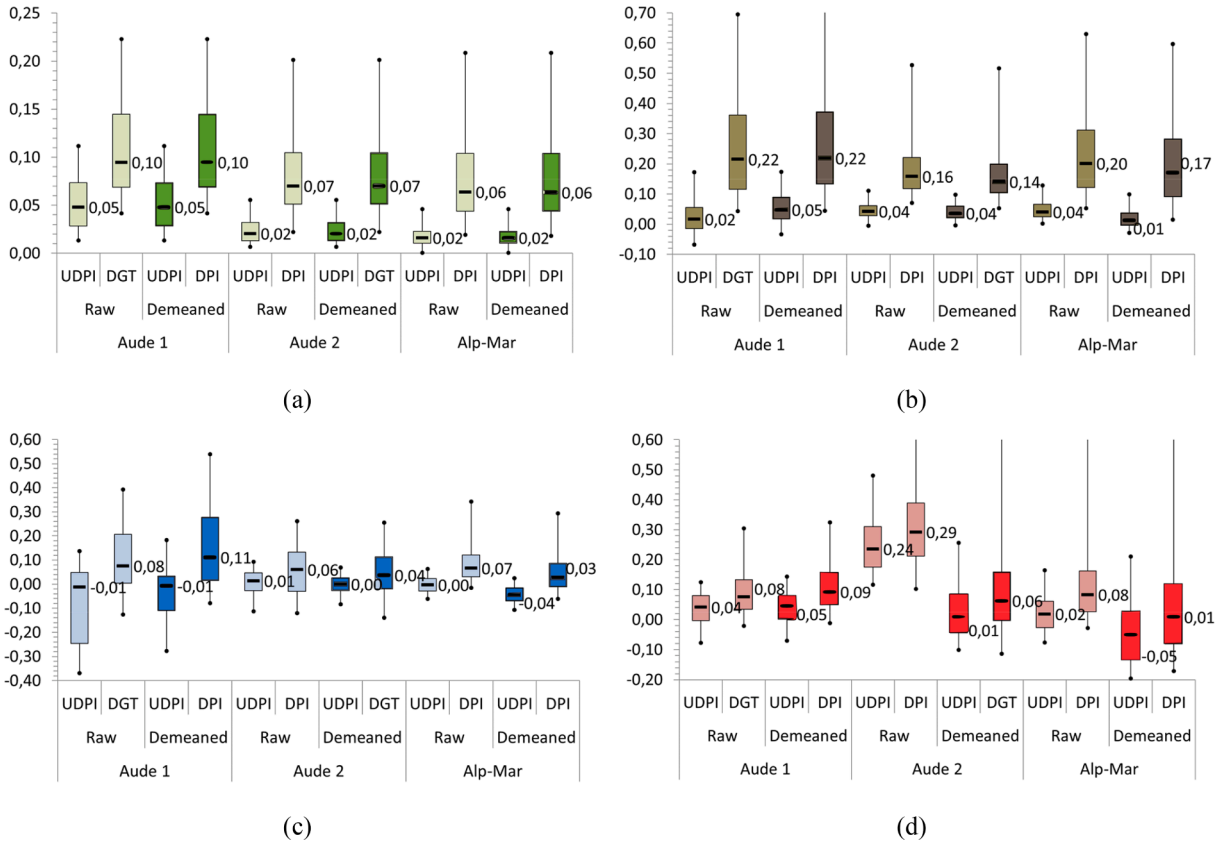

Fig. 9. Boxplot of $(RD^k)_\theta$ distributions (raw and with land use demeaning pre-processing) based on the closest S2 and S1 change images. (a) k = NDVI, θ = standard deviation; (b) k = NDWI, θ = maximum; (c) k = SAVI, θ = mean; (d) k = VV polarization when NDVI < 0.25, θ = maximum.

a specific land cover type, rightful prediction using the raw change images was previously incidental. This method's true potential to single out damaged plots from plot-based pixel statistics of Sentinel change images with coarse spatial resolution (10 m) could thus be lower than initially found. Still, the land use inter-class demeaning pre-processing did allow for good detection efficiency with optimal DPI producer accuracies not falling below 70% while preventing improper identification as much as possible (Fig. 10a and b).

Secondly, including SAR data in the classification process led to heterogeneous results (Table 5). Indeed, $(RD^{VV})_{max}$ seemed fairly complementary to the $[(RD^{NDVI})_{std}; (RD^{SAVI})_{mean}]$ combination, yielding higher DPI accuracy when demeaned pre-processed change images were used. As seen in the bottom of Fig. 10b and on Table 5b, SAR information contributed to detecting a larger amount of damaged plots in *Aude 2* that were not thoroughly identified with optical indices only (DPI accuracy going up from 53% to 70%). On the contrary, with lower scores mostly, SAR brought no additional explanatory power to the association of $(RD^{NDVI})_{std}$ and $(RD^{NDWI})_{max}$ (Table 5a).

Furthermore, contribution of SWIR B11 band from S2 was tested in combination with visible and NIR indices from demeaned change images (Table 6). The addition of $(RD^{B11})_{mean}$ indicator in the classification variables was found more relevant than the use of any $(RD^{NDMI})_\theta$ indicator. Although at a lower native spatial resolution, information from B11 spectral variations allowed enhancing overall results on all three study areas when used with the $[(RD^{NDVI})_{std}; (RD^{SAVI})_{mean}]$ association (Table 6b), closer to what the $[(RD^{NDVI})_{std}; (RD^{NDWI})_{max}]$combination was

Table 5

Overall accuracy, producer accuracy by class and false alarm rates from closest raw and demeaned change images, using visible-NIR indicators only or with $(RD^{VV})_{max}$. Lecture note: *underlined bold* values *indicate that better scores were achieved with the demeaning pre-processed images for a given event (if so, both raw and demeaning scores are tagged). Asterisks indicate best configurations for each event based on lowest false discovery rate, provided that the DPI producer accuracy reaches a reasonable ratio of 70%.*

(a) 1. NDVI - Std 2. NDWI – Max

	550 training plots from *Aude 1* - Oct. 15, 2018: 240 UDPI[1,a] and 310 DGT[1]											
	***Aude 1* - Oct. 15, 2018** 602 validation plots: 240 UDPI[1,b] and 362 DPI[1]				***Aude 2* - May 11, 2020** 681 validation plots: 497 UDPI[2] and 184 DPI[2]				***Alpes-Mar* - Oct. 3, 2020** 1006 validation plots: 571 UDPI[3] and 435 DPI[3]			
	Raw		with demeaning pre-processing		Raw		with demeaning pre-processing		Raw		with demeaning pre-processing	
	Vis-NIR only	Vis-NIR + SAR	Vis-NIR only*	Vis-NIR + SAR	Vis-NIR only	Vis-NIR + SAR	Vis-NIR only*	Vis-NIR + SAR	Vis-NIR only	Vis-NIR + SAR	Vis-NIR only*	Vis-NIR + SAR
Overall accuracy	89%	90%	85%	85%	91%	89%	90%	87%	88%	87%	86%	83%
UDPI	**84%**	86%	**88%**	86%	**92%**	**90%**	**96%**	**93%**	**94%**	**92%**	**99%**	**98%**
DPI	92%	92%	84%	84%	86%	89%	74%	72%	80%	80%	70%	64%
False discovery rate	**10%**	9%	**9%**	10%	**19%**	**24%**	**13%**	**22%**	**9%**	**11%**	**2%**	**4%**
False positive rate	**16%**	**14%**	**12%**	**14%**	**8%**	**10%**	**4%**	**7%**	**6%**	**8%**	**1%**	**2%**

(b) 1. NDVI - Std 2. SAVI - Mean

	550 training plots from *Aude 1* - Oct. 15, 2018: 240 UDPI[1,a] and 310 DGT[1]											
	***Aude 1* - Oct. 15, 2018** 602 validation plots: 240 UDPI[1,b] and 362 DPI[1]				***Aude 2* - May 11, 2020** 681 validation plots: 497 UDPI[2] and 184 DPI[2]				***Alpes-Mar* - Oct. 3, 2020** 1006 validation plots: 571 UDPI[3] and 435 DPI[3]			
	Raw		with demeaning pre-processing		Raw		with demeaning pre-processing		Raw		with demeaning pre-processing	
	Vis-NIR only	Vis-NIR + SAR*	Vis-NIR only	Vis-NIR + SAR	Vis-NIR only	Vis-NIR + SAR	Vis-NIR only	Vis-NIR + SAR*	Vis-NIR only	Vis-NIR + SAR*	Vis-NIR only	Vis-NIR + SAR
Overall accuracy	89%	90%	82%	86%	89%	**88%**	86%	**89%**	83%	83%	79%	81%
UDPI	88%	89%	83%	84%	**95%**	**91%**	**98%**	**96%**	**97%**	**97%**	**100%**	**98%**
DPI	89%	90%	82%	87%	71%	79%	53%	70%	65%	66%	52%	58%
False discovery rate	8%	7%	12%	11%	**15%**	**24%**	**9%**	**14%**	**5%**	**6%**	**0%**	**4%**
False positive rate	12%	11%	17%	16%	**5%**	**9%**	**2%**	**4%**	**3%**	**3%**	**0%**	**2%**

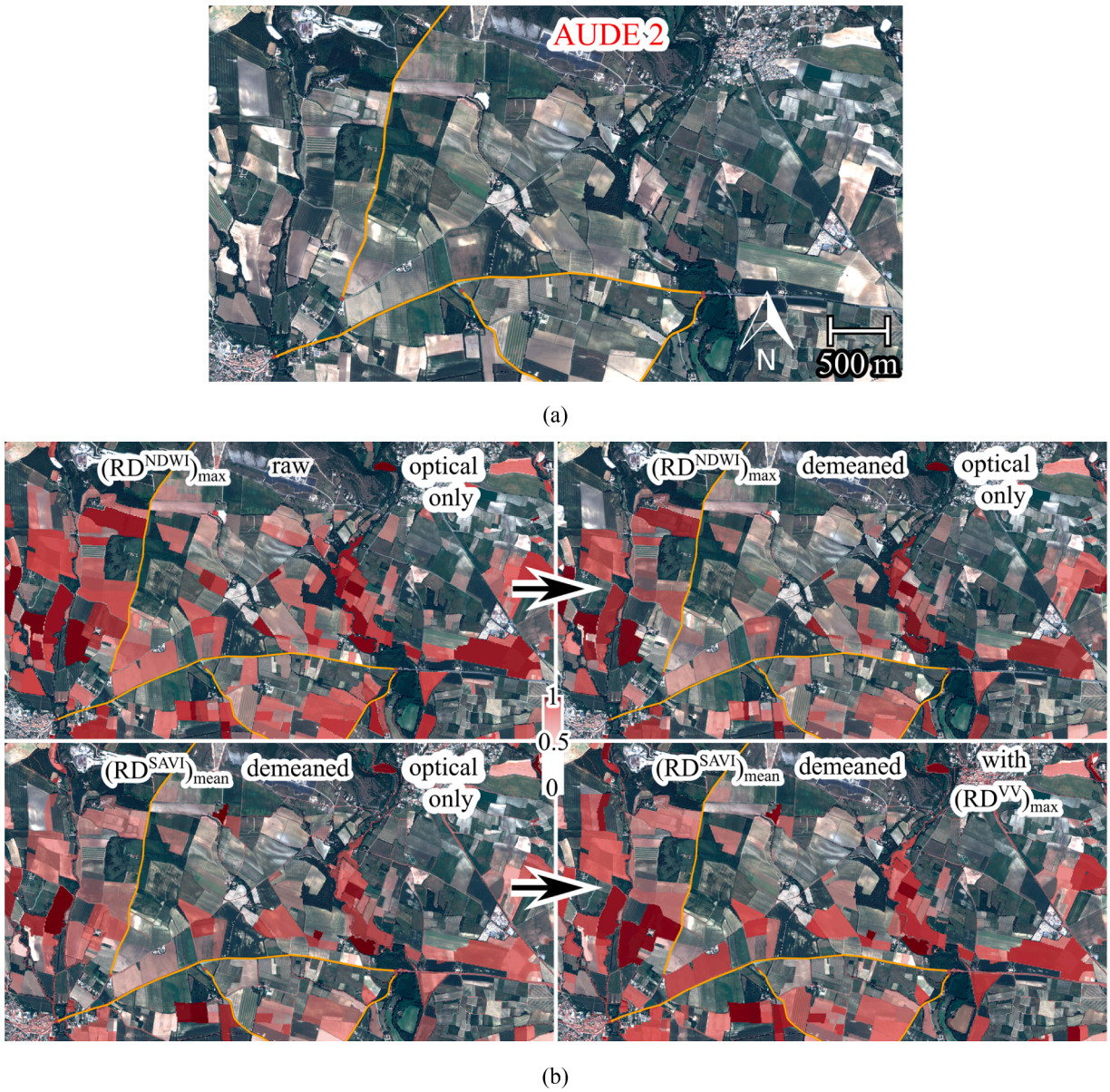

Fig. 10. (a) Close-up example of damages on *Aude 2* event over *Pléiades* image from 2020/05/22; (b) Output map displaying the probability of damage classification by Gaussian Process classifier based on $[(RD^{NDVI})_{std}; X]$ optical combination and improvements.

able to yield on its own (Table 6a). Accounting for SWIR changes particularly allowed decreasing further the false discovery rate (down to 9%) on the *Aude 2* study event (Table 6a). On the contrary, both B11 and NDMI indicators brought slightly degraded performance on the two other events.

Overall, the $[(RD^{NDVI})_{std}; (RD^{NDWI})_{max}]$ combination appeared the most versatile on all three study events, with only marginal to no improvement from the use of SAR $(RD^{VV})_{max}$ or SWIR $(RD^{B11})_{mean}$ indicators. Two demonstrations of satisfying detection capacity can be observed in Fig. 11 using this combination of optical indicators.

3.4. Detection robustness with regards to the availability of optical pre event images

Availability of satellite optical images greatly depends on atmospheric conditions. When investigating heavy rainfall events, persistent cloud cover is usually observed for days before and after the floods. Naturally, the further back in time the pre event images, the more the observed spectral changes are likely to carry multiple signatures from different sources, making them harder to interpret, especially during spring season where vegetation actively regrows. With land use specific demeaning, the pre-processing procedure was expected to help counteract at least some of these unwanted spectral patterns. To quantify this effect and address this concern, multiple S2 change images were created using the closest post event images and pre event acquisitions up to 70 days beforehand. Because damages can be relatively durable (except for those that are rapidly cleaned up), one would expect the use of more distant post event images to be less problematic than pre event images. Thus, detection capacity with regards only to distant pre event images was investigated here. The distributions of the three plot-based optical $(RD^k)_\theta$ indicators from demeaned change images are exhibited in Fig. 12, by class and depending on the time interval between the S2 pre event and closest post event images.

As the interval of time between both images got larger, an increase in the variance of UDPI and DPI distributions was generally observed for all indicators and all study sites, confirming that more numerous sources of spectral changes and thus greater overall disparities were expected over longer periods of time. For each site, $(RD^{NDVI})_{std}$ values (Fig. 12a) were

Table 6
Overall accuracy, producer accuracy by class and false alarm rates from demeaned change images, using visible-NIR indicators only, or either with $(RD^{B11})_{mean}$ or $(RD^{NDMI})_{mean}$. Lecture note: *Asterisks indicate best configurations for each event based on lowest false discovery rate, provided that the DPI producer accuracy reaches a reasonable ratio of 70%.*

(a) 1. NDVI - Std 2. NDWI – Max

	550 training plots from **Aude 1 - Oct. 15, 2018:** 240 UDPI[1,a] and 310 DGT[1]								
	Aude 1 - Oct. 15, 2018 602 validation plots: 240 UDPI[1,b] and 362 DPI[1]			**Aude 2 - May 11, 2020** 681 validation plots: 497 UDPI[2] and 184 DPI[2]			**Alpes-Mar. - Oct. 3, 2020** 1006 validation plots: 571 UDPI[3] and 435 DPI[3]		
	Vis-NIR only*	Vis-NIR + B11	Vis-NIR + NDMI	Vis-NIR only	Vis-NIR + B11*	Vis-NIR + NDMI	Vis-NIR only*	Vis-NIR + B11	Vis-NIR + NDMI
Overall accuracy	85%	83%	84%	90%	90%	91%	86%	83%	85%
UDPI	88%	82%	82%	96%	97%	96%	99%	97%	98%
DPI	84%	84%	85%	74%	69%	77%	70%	65%	69%
False discovery rate	9%	12%	12%	13%	9%	13%	2%	5%	4%
False positive rate	12%	18%	18%	4%	3%	4%	1%	3%	2%

(b) 1. NDVI - Std 2. SAVI - Mean

	550 training plots from **Aude 1 - Oct. 15, 2018:** 240 UDPI[1,a] and 310 DGT[1]								
	Aude 1 - Oct. 15, 2018 602 validation plots: 240 UDPI[1,b] and 362 DPI[1]			**Aude 2 - May 11, 2020** 681 validation plots: 497 UDPI[2] and 184 DPI[2]			**Alpes-Mar. - Oct. 3, 2020** 1006 validation plots: 571 UDPI[3] and 435 DPI[3]		
	Vis-NIR only	Vis-NIR + B11*	Vis-NIR + NDMI	Vis-NIR only	Vis-NIR + B11*	Vis-NIR + NDMI	Vis-NIR only	Vis-NIR + B11*	Vis-NIR + NDMI
Overall accuracy	82%	85%	83%	86%	89%	89%	79%	83%	81%
UDPI	83%	83%	81%	98%	97%	97%	100%	99%	99%
DPI	82%	86%	85%	53%	68%	67%	52%	61%	57%
False discovery rate	12%	12%	13%	9%	10%	10%	0%	2%	2%
False positive rate	17%	17%	19%	2%	3%	3%	0%	1%	1%

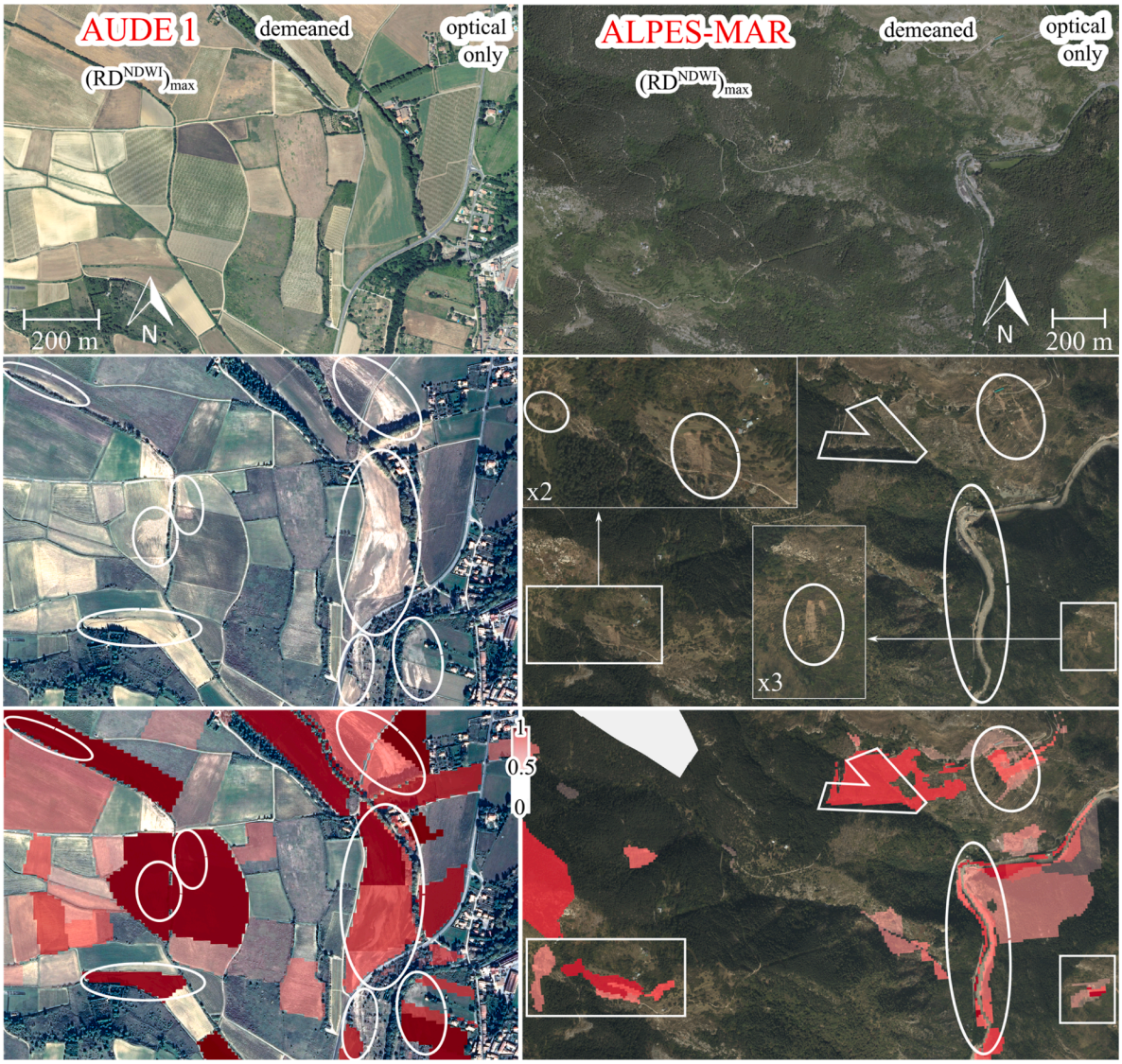

Fig. 11. Close-up examples of damage detection based on $[(RD^{NDVI})_{std}; (RD^{NDWI})_{max}]$ optical combination. Top: Pre event IGN *orthophotos* 2017. Middle: Post event *Pléiades* image or IGN *orthophotos*. Bottom: Resulting mapped hazards by Gaussian Process classifier with probability of damage classification.

progressively tilted upwards illustrating greater intra plot heterogeneities. UDPI and DPI classes remained however pretty well severable. Fairly good separation was also still observed with $(RD^{NDWI})_{max}$ medians (Fig. 12b) remaining globally stable in all study events. However, the $(RD^{SAVI})_{mean}$ indicator (Fig. 12c) was found the most unsteady with largely overlapping distributions between UDPI and DPI classes when considering more distant images, especially for the *Aude 2* event. This could easily be fathomed since this particular storm took place on May 11, during spring time, and the closest cloud free post event image was obtained on May 20. Therefore, the change images produced with pre event data acquired 40 days earlier (April 10) and 63 days earlier (March 18) carried considerable spectral changes due to spring blossom and agricultural practices. The other two events, *Aude 1* and *Alpes-Mar*, occurring in the beginning of October, benefited from several months of far more stable weather and environmental conditions (from July to mid-October).

Classification scores based on demeaned change images as a function of the time interval between the Sentinel-2 pre event and closest post event images can be observed in Table 7.

Overall accuracies were pretty stable for the *Aude 1* and *Alpes-Mar* events. For the latter, they dissimulated lower detection capacity for unaffected areas (UDPI) leading to false discovery rates going from 2% to 8% and for the worst case 18%. Still, rather stable DPI scores were achieved due to steady land cover conditions. Classification performance however significantly dropped for the *Aude 2* site. In particular, the UDPI producer accuracy decreased from more than 96% to 80% and less, leading to false discovery rates up to 57% for the $[(RD^{NDVI})_{std}; (RD^{NDWI})_{max}]$ combination, corroborating that the exploitation of change images between mid-March and mid-May in northern hemisphere mid-latitude countries like France can be misguiding. Surprisingly, greater accuracies were reached with the $[(RD^{NDVI})_{std}; (RD^{SAVI})_{mean}]$ combination using highly distant images (70 days) on the *Aude 1* event (Table 7b). This called for critical evaluation of the selection of plot samples and of the method's performance, which will be discussed in Section 4.2. Nevertheless, the method still appeared reasonably robust as long as stable ground conditions (*Aude 1* and *Alpes-Mar*) were observed between the pre event image and the event itself. As expected, the closer the pre and post event images, the greater discrimination capacity and the lesser false discovery rates in change detection.

Because radar signals can be acquired in any meteorological condition (cloudy and by night), interpretable SAR images can always be obtained in close proximity to a disaster should satellite revisit fre-

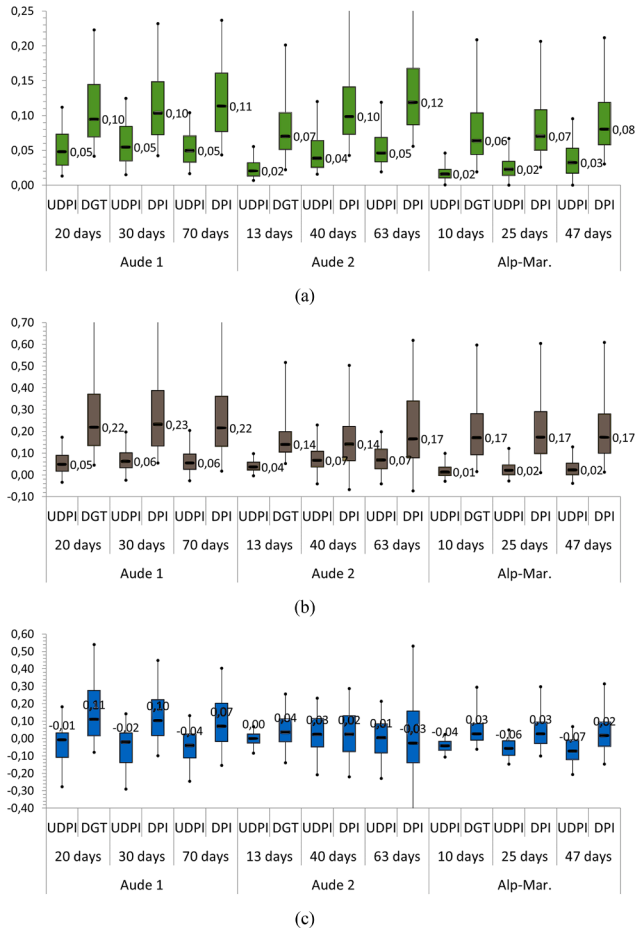

Fig. 12. Boxplot of $(RD^{k})_{\theta}$ distributions from demeaned change images depending on the time interval between the S2 pre event and the closest post event images. (a) k = NDVI, θ = standard deviation; (b) k = NDWI, θ = maximum; (c) k = SAVI, θ = mean.

quency be high enough (around 5 days for S1). In order to restore potentially reduced detection capacities from the use of distant optical change images, the most promising SAR variable, $(RD^{VV})_{max}$, still derived from the closest S1 demeaned change images was also tested in combination with the demeaned optical indicators. Scores from Table 7 show that for the $[(RD^{NDVI})_{\mathrm{std}};\ (RD^{NDWI})_{\mathrm{max}}]$ combination, SAR data mostly restored slightly greater UDPI and DPI producer accuracies on the Aude study sites. It was not the case for DPI in *Alpes-Mar*. This result was consistent with conclusions on SAR contribution derived from Table 5 and confirmed that either (i) all the available explanatory power was already carried by optical information on *Alpes-Mar* or (ii) radar signals might be much less interpretable or relevant on a steep mountainous woodland region. It could be explained by the presence of complex topography and the fact that, given the quantities of rainfall involved (500 mm+) in such a short time period, most damages observed on the high slopes likely originated from Horton overland flow, or alternatively that most of the soils in the whole area, damaged or not, were saturated likewise (Carrega and Michelot, 2021). Finally, although the introduction of SAR data might have helped marginally on agricultural areas like those of the Aude department, it turned out to be unable to fully recover the detection ability derived from closest optical images.

3.5. Cross-site training

In the previous subsections of Section 3, only one training configuration based on *Aude 1* data was tested. Here, a cross-site validation approach was set up using *Alpes-Mar* or *Aude 2* classes instead of *Aude 1* as training sample. Results are displayed in Table 8 using the closest demeaned optical change images on the two remaining validation samples. UDPI producer accuracy was found very poor on *Aude 1* with only 50% of the unaffected areas correctly classified when *Alpes-Mar* was used as training (column (a) of Table 8), indicating massive damage overestimations. This could be related to higher values and a larger variance for all three demeaned optical indicators on *Aude 1* unaffected plots (Fig. 9). A close although weaker outcome was observed on *Aude 2* (column (b) of Table 8) with large numbers of false discoveries, or comparatively when *Aude 2* was used as training to perform detection on *Aude 1* (column (c) of Table 8). The most likely explanation was that *Aude 1* change image, and to a lesser extent *Aude 2*'s, intrinsically displayed more variety in patterns of spectral changes than *Alpes-Mar* data samples, which in turn stemmed from Aude's landscape featuring much more various types of soils in different growing conditions (see Fig. 6 or Fig. 13). In addition, *Aude 1* change image was derived from more distant acquisitions than *Aude 2*, and even more than *Alpes-Mar* (20, 13 and 10 days respectively). Global spectral variations were thus more pronounced on *Aude 1* than on the two other sites. This led to the classifier trained on *Alpes-Mar* or *Aude 2* being scarcely able to recognize *Aude 1* UDPI plots as carrying so much inner variability and wrongly tagging too many of them as damaged. Because these variabilities were partly present on homogeneous land covers, the demeaning preprocessing was unable to efficiently smooth this effect. Finally, classification accuracies on *Alpes-Mar* using the $[(RD^{NDVI})_{\mathrm{std}};\ (RD^{NDWI})_{\mathrm{max}}]$ combination and *Aude 2* as learning sample (column (d) of Table 8) turned out to be very close to those obtained using *Aude 1* (99% UDPI, 70% DPI, 2% false discoveries versus 97%, 71% and 6% here), highlighting some robustness in the methodology between *Aude 1* and *Aude 2* demeaned samples.

As seen in the result Sections 3.1 and 3.3, detection of *Alpes-Mar* and *Aude 2* damaged areas was satisfactory using *Aude 1* as training data (70% and 74% respectively with $<$ 4% false positives). This has great implications for land cover change detection replicability based on statistical methods in general. It could be concluded that when using a Gaussian process type classifier, suitable detection of damaged areas should better be carried out using UDPI learning classes featuring slightly more inherent variabilities than the test ones, which in turn should also partly rely on using more distant change images for training. That may however lead to plots with small damages bearing weak spectral signatures being mistaken as unaffected. Therefore, eventually for this method to be fully and more satisfactorily replicable, a handful of different training samples could be set up depending on the type of region to be analysed (multi agricultural areas, mountainous woodlands) and on the time distance between the pre and post event acquisitions.

4. Discussion

4.1. Detection accuracy

Various remote sensing studies have implemented change detection techniques through thresholding, change vector and principal component analysis or supervised classification to identify areas affected by flood and erosion or assess landslide occurrence after heavy rainfall events. For instance, Dhakal et al. (2002) reached 88% overall accuracy using Landsat TM data on a small-size watershed in Nepal. However, they only had 94 ground truths reference data (among which 50 from affected areas) to assess the accuracy of their method. In this study, more than 2800 land cadastre plots over the three study areas served for training/accuracy assessment, emphasizing the robustness of the results.

In other works, Byun et al. (2015) obtained from bi-temporal KOMPSAT-2 VHR images an overall accuracy of 75% and a false discovery rate (also referenced as commission error) of 33.5% to detect flooded areas in the city of N'djamena in Chad. Using a Random Forest classifier with both S2 and S1 pre and post event data, Kocaman et al.

Table 7
Overall accuracy, producer accuracy by class and false alarm rates from demeaned change images depending on the time interval between the S2 pre event and closest post event images, using visible-NIR indicators only or with $(RD^{VV})_{max}$. *Lecture note: underlined bold values indicate that better scores were achieved including the $(RD^{VV})_{max}$SAR indicator among the classification variables for a given event (if so, both visible-NIR and visible-NIR + SAR scores are tagged).*

(a) 1. NDVI - Std 2. NDWI – Max

	550 training plots from *Aude 1* - Oct. 15, 2018: 240 UDPI[1,a] and 310 DGT[1]																	
	***Aude 1* - Oct. 15, 2018** 602 validation plots: 240 UDPI[1,b] and 362 DPI[1]						***Aude 2* - May 11, 2020** 681 validation plots: 497 UDPI[2] and 184 DPI[2]						***Alpes-Mar* - Oct. 3, 2020** 1006 validation plots: 571 UDPI[3] and 435 DPI[3]					
	Vis-NIR only			Vis-NIR + SAR			Vis-NIR only			Vis-NIR + SAR			Vis-NIR only			Vis-NIR + SAR		
Interval of time in optical change image for validation (days)	20	30	70	20	30	70	13	40	63	13	40	63	10	25	47	10	25	47
Overall accuracy	85%	**82%**	**85%**	85%	**85%**	**85%**	90%	**74%**	**68%**	87%	**77%**	**72%**	86%	86%	82%	83%	83%	82%
UDPI	88%	**85%**	**88%**	86%	**85%**	**89%**	96%	**80%**	**71%**	93%	**83%**	**76%**	99%	**95%**	**87%**	98%	**95%**	**92%**
DPI	**84%**	**80%**	**82%**	**84%**	**84%**	**83%**	74%	**57%**	**60%**	72%	**63%**	**61%**	70%	73%	76%	64%	66%	68%
False discovery rate	9%	**11%**	**9%**	10%	**11%**	**8%**	13%	**49%**	**57%**	22%	**43%**	**51%**	2%	8%	**18%**	4%	9%	**13%**
False positive rate	12%	**15%**	**12%**	14%	**15%**	**11%**	4%	**20%**	**29%**	7%	**17%**	**24%**	1%	**5%**	**13%**	2%	**5%**	**8%**

(b) 1. NDVI - Std 2. SAVI - Mean

	550 training plots from *Aude 1* - Oct. 15, 2018: 240 UDPI[1,a] and 310 DGT[1]																	
	***Aude 1* - Oct. 15, 2018** 602 validation plots: 240 UDPI[1,b] and 362 DPI[1]						***Aude 2* - May 11, 2020** 681 validation plots: 497 UDPI[2] and 184 DPI[2]						***Alpes-Mar* - Oct. 3, 2020** 1006 validation plots: 571 UDPI[3] and 435 DPI[3]					
	Vis-NIR only			Vis-NIR + SAR			Vis-NIR only			Vis-NIR + SAR			Vis-NIR only			Vis-NIR + SAR		
Interval of time in optical change image for validation (days)	20	30	70	20	30	70	13	40	63	13	40	63	10	25	47	10	25	47
Overall accuracy	**82%**	**82%**	86%	**86%**	**83%**	85%	**86%**	79%	76%	**89%**	77%	73%	**79%**	81%	**79%**	**81%**	81%	**81%**
UDPI	**83%**	82%	88%	**84%**	81%	88%	98%	83%	80%	96%	78%	73%	100%	96%	94%	98%	95%	92%
DPI	**82%**	81%	84%	**87%**	85%	84%	**53%**	**70%**	**65%**	**70%**	**73%**	**71%**	**52%**	62%	**59%**	**58%**	62%	**66%**
False discovery rate	**12%**	**13%**	9%	**11%**	**13%**	9%	9%	40%	45%	14%	45%	50%	0%	8%	11%	4%	10%	13%
False positive rate	**17%**	18%	12%	**16%**	19%	13%	2%	17%	20%	4%	22%	27%	0%	4%	6%	2%	5%	8%

Table 8
Overall accuracy, producer accuracy by class and false alarm rates from closest demeaned change images using optical indicators only and using *Alpes-Mar* or *Aude 2* data as training sample.

	1006 training plots from ***Alpes-Mar*** - **Oct. 3, 2020**: 571 UDPI[3] and 435 DPI[3]				681 training plots from ***Aude 2*** - **May 11, 2020**: 497 UDPI[2] and 184 DPI[2]			
	Aude 1 - **Oct. 15, 2018** 602 validation plots: 240 UDPI[1,b] and 362 DPI[1] (a)		***Aude 2*** - **May 11, 2020** 681 validation plots: 497 UDPI[2] and 184 DPI[2] (b)		***Aude 1*** - **Oct. 15, 2018** 602 validation plots: 240 UDPI[1,b] and 362 DPI[1] (c)		***Alpes-Mar*** - **Oct. 3, 2020** 1006 validation plots: 571 UDPI[3] and 435 DPI[3] (d)	
Optical indicators $(RD^k)_\theta$ combination	1. NDVI - Std 2. NDWI - Max	1. NDVI - Std 2. SAVI - Mean	1. NDVI - Std 2. NDWI - Max	1. NDVI - Std 2. SAVI - Mean	1. NDVI - Std 2. NDWI - Max	1. NDVI - Std 2. SAVI - Mean	1. NDVI - Std 2. NDWI - Max	1. NDVI - Std 2. SAVI - Mean
Overall accuracy	77%	80%	86%	82%	83%	77%	85%	83%
UDPI	46%	51%	84%	79%	75%	56%	97%	98%
DPI	98%	98%	92%	91%	88%	91%	71%	63%
False discovery rate	27%	25%	32%	38%	16%	24%	6%	4%
False positive rate	54%	49%	16%	21%	25%	44%	3%	2%

(2020) reached around 90% overall correct classification to discriminate flooded areas on one case study in Turkey. Landslide susceptibility was also achieved but without the use of satellite products. Pulvirenti et al. (2020) showed that clustering and thresholding techniques using S2 multitemporal data allowed obtaining 91% overall accuracy and 12% false discovery rate in identifying flood pixels during the Northern Queensland (Australia) February 2019 event. Furthermore, semi-automated landslide detection combining object-based image analysis and support vector machine classifier on a single GeoEye-1 multispectral image yielded 95% producer accuracy and a false discovery rate below 26% in Madeira Island (Heleno et al., 2016). In this study, various kinds of extreme rainfall-related disturbances from overflowing to mudslides, landslides and vegetation uprooting, were successfully discriminated using S2 optical and S1 radar data, as well as plot delineation and land cover information. More than 85% overall accuracy and no more than 13% false discovery rate was achieved on three distinct events using only one training sample from one of them. Taking into account the need for adequate unaffected training classes discussed in Section 3.5, such precision is particularly satisfying and encouraging to perform future detection in other areas without requiring additional training data.

4.2. Plot selection bias and territorial subdivision

Complementing ground truths obtained from various sources, photo-interpretation of VHR images was crucial to validating the method presented in this paper. Although most deteriorations were pretty well recognizable, especially on the *Alpes-Mar* site thanks to the post event airborne *orthophotos* from IGN at 0.15 m resolution, some were subject to our own interpretations. Should photo-interpretation have been performed by another operator, DPI samples would have certainly turned out to be slightly different, particularly in the Aude department. Indeed, sizable heterogeneities and color patterns were sometimes present (e.g. Fig. 13), leading to potential misjudgements and thus biases towards indicating unaffected plots as damaged (much less the other way around). Such misinterpretation in turn could explain how both better UDPI and DPI accuracies were reached with more distant images on *Aude 1* (see Table 7b, 70 days versus 20 days, optical only). Indeed, rightful classification of plots falsely categorized in DPI classes may have been greater due to higher likeliness of detecting unusual patterns on longer periods.

The assumption about land use homogeneity inside land cadastre plots was critical in this approach. Indeed, each land cover changes in distinctive ways depending on the time of the year and can react very differently to heavy precipitation. As a consequence, a plot containing two contrasting land covers could present high disparity in change pixels even though no significant change occurred due to the extreme weather event between the two acquisition dates. Step 2.a described in Section 2.5 thus appeared appealing within the demeaning pre-processing to correct this effect on plots with several overlaying land covers. On the other hand, when the images were close enough in time (which was particularly the case for *Alpes-Mar*), unaffected plots usually bore neutral responses over their whole extent ($RD^k \sim 0$), even with different types of land cover. Step 2.b was therefore chosen for the land use demeaning procedure so that no artificial disparities were introduced inside these unchanged plots. As a consequence, some plots made of several land use categories or lineaments were sometimes tagged in the resulting probability maps (Fig. 13).

Because the land cadastre featured great variability in plot dimension and change detection relied on fixed pixel size (10 m), large plots were sometimes overlooked (Fig. 14). Indeed, with intra-plot pixel statistics as classification variables, plot size played a major role in detection capacity, with mean and standard deviation of change pixels being greatly dependent on damage extent in proportion to plot area. The larger the plots, the more small damages could be characterized by values of $(RD^k)_{\text{std}}$ or $(RD^k)_{\text{mean}}$ falling in the same range as other

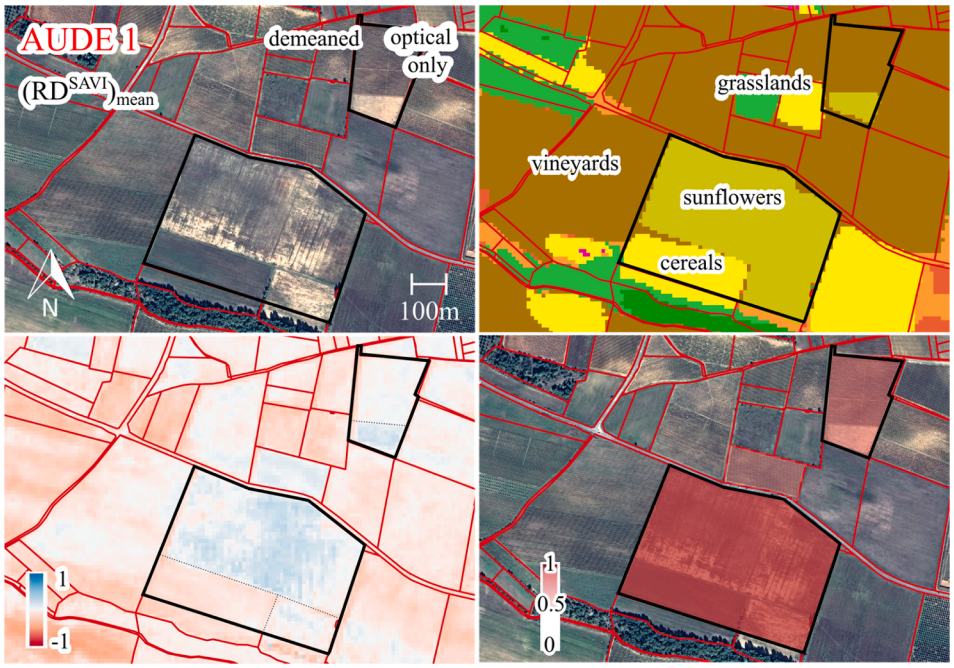

Fig. 13. Example of plots incorrectly flagged as damaged by the classifier because of distinctive reactions between mixed land use types. Top left: *Pléiades* true colors Nov. 3, 2018, post event. Top right: OSO land cover on land cadastre. Bottom left: S2 demeaned RD^{NDVI} Oct. 5–25. Bottom right: Resulting mapped damages by Gaussian Process classifier. Top left image illustrates the difficulty in photo-interpreting potential damages. Bottom left figure shows great disparity in *Aude 1* RD^{NDVI} pixels, even after plot-wise demeaning.

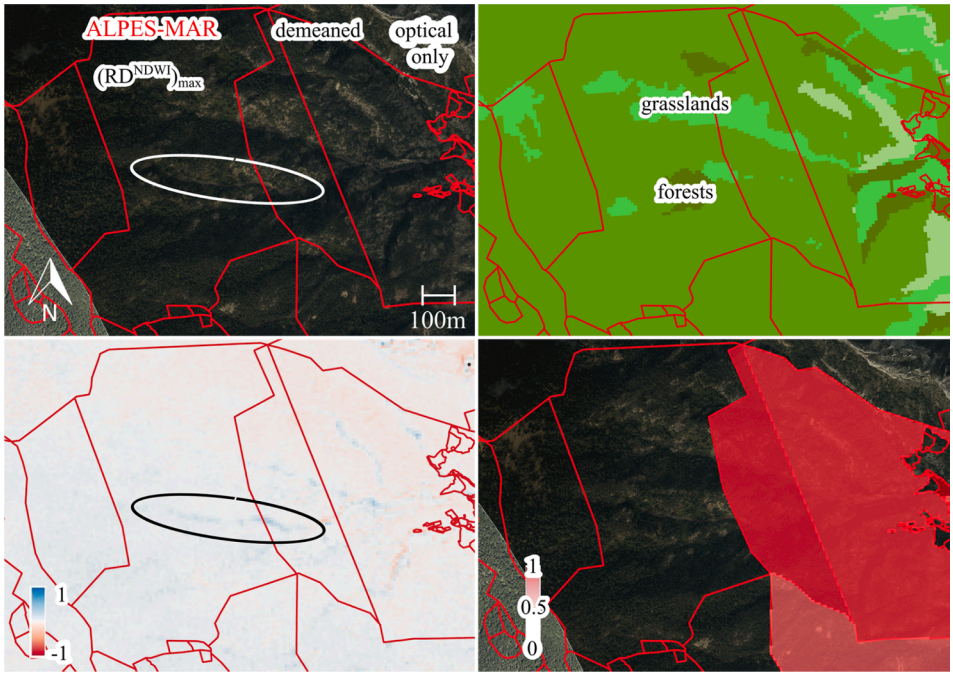

Fig. 14. Example of mudslides undetected on the centre left plot due to cadastre subdivision. Top left: IGN *orthophotos* Oct. 5, 2020, post event. Top right: OSO land cover on land cadastre. Bottom left: S2 demeaned RD^{NDVI} Sept. 28 - Oct. 8. Bottom right: Resulting mapped damages by Gaussian Process classifier.

"average" plots. Only the use of the $(RD^k)_{max}$ indicator allowed avoiding such biases, despite also wrongly inducing damage classification based on single isolated change pixels. In related terms, roads covered in mud or small overflowing deposits were sometimes unidentified, for they could lie in-between land cadastre plots (see for example Fig. 13).

4.3. Spatial resolution of satellite products and VHR post-processing

As in all studies involving detection from remote sensing imagery, results were highly dependent on the spatial resolutions at stake. First, if land surface patterns were very well discernible on IGN *orthophotos* with 15 cm resolution, *Pléiades* images were sometimes harder to interpret, even with a 50 cm resolution, especially when images were acquired with large viewing angles and when small scale damages were involved. Sentinel images, providing pixel information at 10 m ground range, obviously bore great limitations in terms of detection capacity, for instance to identify gullies that are a few meters wide at the most. The methodology developed in this study rather relied upon the statistical likeliness that most damaged plots featured singular variations in coarse neighboring pixels. This was obvious for plots with large scale damages that were able to stand out at the scale of Sentinel pixels but it was more questionable for smaller ones. Obviously, if optical and SAR imagery

with higher spatial resolution were available at a comparable or higher revisit frequency (a few days), new evaluations should be carried out. Nevertheless, the finer the resolution the greater the number of pixels and thus the variability of spectral information contained in a single plot. In order to obtain better results, damage signatures would have to be more prominent than other natural and possibly confounding artifacts on the fine-scale change pixels. With multitemporal VHR images, increased attention would have to be paid to co-registration, and an effective modeling of spatial context in neighboring pixels would be required to accurately capture change information (see Saha et al., 2019, for instance).

For now, most VHR products are not continuously acquired and are thus only available after natural disasters. Therefore, they often can't be used for change detection (or only with very distant images). Still, Yésou et al. (2015a, 2015b) and Huber et al. (2013) proved that accurate detection capacity could be reached using only post disaster *Pléiades* products. Hence, they could rather be of service in a post-processing step within plots already identified using the coarser Sentinel-based change detection method developed here. Patch-based semantic segmentation could be performed to refine damage identification (e.g. Basnyat et al., 2021, on floods or Brand and Manandhar, 2021, on wildfires) and overcome cadastre subdivision issues (Fig. 13). Unsupervised deep learning techniques with convolutional neural networks (CNN) could also be tested as they proved relevant for large-scale mapping of floods (Jiang et al., 2021).

This work aimed at deriving suitable indicators that can reliably provide statistical likeliness of damage evidence without *a priori* assumptions on the shapes of damages. Further detection capacity, for example aiming at discriminating the different types of deteriorations such as gullies or landslides, could be developed through the use of more advanced algorithms allowing for pattern recognition, considering that intense overland flow mostly occurs along continuous lines and perpendicularly to topographical contour levels.

5. Conclusions

Various types of land surface deteriorations arise in the aftermath of extreme hydro-meteorological events. While the vast majority of research and operational activities to date have focused on the most familiar type of flood-related degradations, i.e. overflowing in the vicinity of active rivers, an original approach aiming at identifying large-scale evidence of intense overland flow of rainwater was developed in this work. Because actual intense rainwater runoff is hardly ever observable, focus was made on detecting its resulting footprints at the ground. Plot delineation and land use information were combined to high temporal resolution optical (Sentinel-2) and SAR (Sentinel-1) open-source data to design and test an automatic and repeatable plot-based change detection method on three major storms in the Aude and Alpes-Maritimes departments in the South of France. Based on ground truths confirmed by photo-interpretation of VHR optical imagery and a unique training sample from one study site, a supervised classification algorithm involving statistical patterns in the temporal variations of spectral indices allowed successful discrimination of damaged plots. A demeaning pre-processing of the images by land use type led to more unequivocal results on the method's potential to single out various kinds of deteriorations in contrasted environments from satellite imagery with 10 m spatial resolution. The $[(RD^{NDVI})_{std}; (RD^{NDWI})_{max}]$ combination yielded highest overall accuracies and false positive rates on all three events (at least 85% and 12% respectively). The benefits of introducing SWIR in addition to visible and near-infrared indices were limited to a few percentage points. SAR-derived proxies of soil moisture and roughness were found consistent with the presence of weakly vegetated damaged areas, with VV being the most sensitive polarization. Nonetheless, additional classification accuracy was not significantly reached with S1 data as compared to the exclusive use of S2. Although good results were reached on all three events with a unique training sample, performance of the method was found conditional to the use of change images displaying more inherent time variabilities in the unaffected learning plots than in the test ones. Such conditions should be partly met by using more distant images to derive the training dataset than for the assessed event.

For post disaster operational needs, reasonable reliability in ordering relief interventions or in helping the certification of disaster claims could be achieved with false discovery rates below 13%. In terms of prevention, such detection accuracy will allow evaluating and improving diagnostic methods for mapping intense runoff spatial hazard. Relying on similar principles as data assimilation in meteorology, detection of actual historical damages in a given region would allow creating proxy databases. Extreme overland flow susceptibility indicators, currently inferred from terrestrial data (topography, land use, soil type), could thus be further fine-tuned using non redundant information from remote sensing. Besides, future research will aim at providing refined identification capacity and at differentiating the different types of deteriorations at an intra-plot scale, for instance by using U-net CNN with VHR post event data. This work could also turn out to be very helpful in other parts of the world such as tropical regions, and especially mountainous islands, which are even more exposed to intense overland flow risks induced by repeated extreme weather events. For this, the high temporal resolution of Sentinel-2 could provide sufficient coverage to circumvent the enduring cloudy conditions. Should close optical images still be hard to come by at these latitudes, VHR SAR products such as TerraSAR-X might be able to help restoring slightly better detection capabilities.

Declaration of Competing Interest

The authors declare that they have no known competing financial interests or personal relationships that could have appeared to influence the work reported in this paper.

Acknowledgments

The authors would like to thank Hervé Yésou (SERTIT) for his expertise on *Pléiades* data and for valuable research guidance in the mapping of damages caused by natural disasters using very high resolution optical imagery. We are also grateful to Aude's *Direction Départementale des Territoires et de la Mer* (DDTM 11) for providing precious ground truths data. This work was supported by DGPR/SRNH grant n°21367400 for the 2021 field campaign to the Roya and Vésubie valleys following the "*Alex*" storm.

References

Amarnath, G., Ameer, M., Aggarwal, P., Smakhtin, V., 2012. Detecting spatio-temporal changes in the extent of seasonal and annual flooding in South Asia using multi-resolution satellite data. In: Proc. SPIE 8538, Earth Resources and Environmental Remote Sensing/GIS Applications III, 853818. https://doi.org/10.1117/12.974653.

Baghdadi, N., Cerdan, O., Zribi, M., Auzet, V., Darboux, F., El Hajj, M., Kheir, R.B., 2008. Operational performance of current synthetic aperture radar sensors in mapping soil surface characteristics in agricultural environments: application to hydrological and erosion modeling. Hydrol. Process. 22 (1), 9–20. https://doi.org/10.1002/hyp.6609.

Baghdadi, N., Zribi, M., 2016. Microwave Remote Sensing of Land Surfaces: Techniques and Methods. ISTE Press: London, UK; Elsevier: Oxford, UK, pp.448. ISBN 978178548159.

Basnyat, B., Roy, N., Gangopadhyay, A., 2021. Flood Detection using Semantic Segmentation and Multimodal Data Fusion. In: 2021 IEEE International Conference on Pervasive Computing and Communications Workshops and other Affiliated Events, pp. 135–140. https://doi.org/10.1109/PerComWorkshops51409.2021.9430985.

Begueria, S., 2006. Identifying erosion areas at basin scale using remote sensing data and GIS: a case study in a geologically complex mountain basin in the Spanish Pyrenees. Int. J. Remote Sens. 27, 4585–4598. https://doi.org/10.1080/01431160600735640.

Bell, F.C., Kar, S.O., 1969. Characteristic response times in design flood estimation. J. Hydrol. 8 (2), 173–196. https://doi.org/10.1016/0022-1694(69)90120-6.

Bousbih, S., Zribi, M., Lili-Chabaane, Z., Baghdadi, N., El Hajj, M., Gao, Q., Mougenot, B., 2017. Potential of Sentinel-1 radar data for the assessment of soil and cereal cover parameters. Sensors 17 (11), 2617. https://doi.org/10.3390/s17112617.

Brakenridge, R., Anderson, E., 2006. Modis-based flood detection, mapping and measurement: the potential for operational hydrological applications. In: Marsalek, J., Stancalie, G., Balint, G. (Eds.), Transboundary Floods: Reducing Risks Through Flood Management. Nato Science Series: IV: Earth and Environmental Sciences, vol. 72. Springer, Dordrecht. https://doi.org/10.1007/1-4020-4902-1_1.

Brand, A.K., Manandhar, A., 2021. Semantic segmentation of burned areas in satellite images using a U-net-based convolutional neural network. Int. Arch. Photogramm. Remote Sens. Spatial Inf. Sci. XLIII-B3-2021, 47–53. https://doi.org/10.5194/isprs-archives-XLIII-B3-2021-47-2021.

Breil, P., Lagadec, L.R., Gonzalez-Sosa, E., 2016. Inondation pluviale et développement périurbain. *Novatech 2016.*

Byun, Y., Han, Y., Chae, T., 2015. Image fusion-based change detection for flood extent extraction using Bi-temporal very high-resolution satellite images. Remote Sens. 7, 10347–10363. https://doi.org/10.3390/- rs70810347.

Carrega, P., Michelot, N., 2021. Une catastrophe hors norme d'origine météorologique le 2 octobre 2020 dans les montagnes des Alpes-Maritimes. Physio-Géo 16, 1–70. https://doi.org/10.4000/physio-geo.12370.

Cerbelaud, A., Favro, A., Roupioz, L., Blanchet, G., Briottet, X., Delvit, J.-M., Breil, P., 2020. Potential of high resolution satellite optical imagery to detect damages following extreme rainfall events. La Houille Blanche 6, 66–74. https://doi.org/10.1051/lhb/2020059.

Cerbelaud, A., Roupioz, L., Blanchet, G., Breil, P., Briottet, X., 2021. Supervised classification methods for automatic damage detection caused by heavy rainfall using multitemporal high resolution optical imagery and auxiliary data. Int. Arch. Photogramm. Remote Sens. Spatial Inf. Sci. XLIII-B3-2021, 693–700. https://doi.org/10.5194/isprs-archives-XLIII-B3-2021-693-2021.

Cerdà, A., Novara, A., Dlapa, P., López-Vicente, M., Úbeda, X., Popović, Z., Mekonnen, M., Terol, E., Janizadeh, S., Mbarki, S., Saldanha Vogelmann, E., Hazrati, S., Sannigrahi, S., Parhizkar, M., Giménez-Morera, A., 2021. Rainfall and water yield in Macizo del Caroig, Eastern Iberian Peninsula. Event runoff at plot scale during a rare flash flood at the Barranco de Benacancil. Cuadernos de Investigación Geográfica 47.

Chen, A., Darbon, J., De Franchis, C., Facciolo, G., Meinhardt, E., Michel, J., Morel, J.-M., 2015. Numerical simulation of landscape evolution and water run-off on digital elevation models obtained from Pleiades. Revue Française De Photogrammétrie Et De Télédétection 209, 117–123. https://doi.org/10.52638/rfpt.2015.135.

Danneels, G., Pirard, E., Havenith, H.B., 2007. Automatic landslide detection from remote sensing images using supervised classification methods. In: IEEE International Geoscience and Remote Sensing Symposium, pp. 3014–3017. https://doi.org/10.1109/IGARSS.2007.4423479.

DeVries, B., Huang, C., Armston, J., Huang, W., Jones, J.W., Lang, M.W., 2020. Rapid and robust monitoring of flood events using Sentinel-1 and Landsat data on the Google Earth Engine. Remote Sens. Environ. 240, 111664. https://doi.org/10.1016/j.rse.2020.111664.

Dhakal, A.S., Amada, T., Aniya, M., Sharma, R.R., 2002. Detection of areas associated with flood and erosion caused by a heavy rainfall using multitemporal Landsat TM data. Photogramm. Eng. Remote Sens. 68 (3), 233–239.

Dubucq, M., 1986. Télédétection spatiale et Erosion des sols. Etude bibliographique. Cah. ORSTOM, sér. Pédol. 22 (2), 247–258.

Dwivedi, R.S., Kumar, A.B., Tewari, K.N., 1997. The utility of multi-sensor data for mapping eroded lands. Int. J. Remote Sens. 18 (11), 2303–2318. https://doi.org/10.1080/014311697217620.

Fadul, H.M., Salih, A.A., Ali, I.A., Inanaga, S., 1999. Use of remote sensing to map gully erosion along the Atbara River, Sudan. Int. J. Appl. Earth Obs. Geoinf. 1 (3–4), 175–180. https://doi.org/10.1016/S0303-2434(99)85010-7.

Filipponi, F., 2019. Sentinel-1 GRD preprocessing workflow. Proceedings 18 (1), 11.

Gao, B.C., 1996. NDWI – a normalized difference water index for remote sensing of vegetation liquid water from space. Remote Sens. Environ. 58 (3), 257–266. https://doi.org/10.1016/S0034-4257(96)00067-3.

Gao, Q., Zribi, M., Baghdadi, N., Escorihuela, M.J., 2017. Synergetic use of sentinel-1 and sentinel-2 data for soil moisture mapping at 100 m resolution. Sensors 17 (9), 1966. https://doi.org/10.3390/s17091966.

Goffi, A., Stroppiana, D., Brivio, P.A., Bordogna, G., Boschetti, M., 2020. Towards an automated approach to map flooded areas from Sentinel-2 MSI data and soft integration of water spectral features. Int. J. Appl. Earth Obs. Geoinf. 84, 101951. https://doi.org/10.1016/j.jag.2019.101951.

Heleno, S., Matias, M., Pina, P., Sousa, A.J., 2016. Semiautomated object-based classification of rain-induced landslides with VHR multispectral images on Madeira Island. Nat. Hazards Earth Syst. Sci. 16, 1035–1048. https://doi.org/10.5194/nhess-16-1035-2016.

Horton, R., 1933. The role of infiltration in the hydrologic cycle. In: Transactions of the American Geophysics Union, 14th Annual Meeting, pp. 446–460.

Horton, Robert E., 1945. Erosional development of streams and their drainage basins; Hydrophysical approach to quantitative morphology. Geol. Soc. Am. Bull. 56 (3), 275–370. https://doi.org/10.1130/0016-7606.

Hostache, R., Puech, C., Raclot, D., 2007. Caractérisation spatiale de l'aléa inondation à partir d'images satellites RADAR. Cybergeo: Eur. J. Geogr. 381 https://doi.org/10.4000/cybergeo.7722.

Huang, F., Chen, L., Yin, K., Huang, J., Gui, L., 2018. Object-oriented change detection and damage assessment using high-resolution remote sensing images, Tangjiao Landslide, Three Gorges Reservoir, China. Environ. Earth Sci. 77, 183. https://doi.org/10.1007/s12665-018-7334-5.

Huber, C., Battiston, S., Yésou, H., Tinel, C., Laurens, A., Studer, M., 2013. Synergy of VHR pleiades data and SWIR spectral bands for flood detection and impact assessment in urban areas: Case of Krymsk, Russian Federation, in July 2012. In: IEEE International Geoscience and Remote Sensing Symposium 2013, pp. 4538–4541. https://doi.org/10.1109/IGARSS.2013.6723845.

Inglada, J., 2018. Contextual version of the OSO 2018 product. Centre d'Expertise Scientifique «CES Occupation des sols». http://osr-cesbio.ups-tlse.fr/~oso/.

Jiang, X., Liang, S., He, X., Ziegler, A.D., Lin, P., Pan, M., Wang, D., Zou, J., Hao, D., Mao, G., Zeng, Y., Yin, J., Feng, L., Miao, C., Wood, E.F., Zeng, Z., 2021. Rapid and large-scale mapping of flood inundation via integrating spaceborne synthetic aperture radar imagery with unsupervised deep learning. ISPRS J. Photogramm. Remote Sens. 178, 36–50. https://doi.org/10.1016/j.isprsjprs.2021.05.019.

Jiao, X., Kovacs, J.M., Shang, J., McNairn, H., Walters, D., Ma, B., Geng, X., 2014. Object-oriented crop mapping and monitoring using multi-temporal polarimetric RADARSAT-2 data. ISPRS J. Photogramm. Remote Sens. 96, 38–46. https://doi.org/10.1016/j.isprsjprs.2014.06.014.

Kharin, V.V., Zwiers, F.W., Zhang, X., Hegerl, G.C., 2007. Changes in temperature and precipitation extremes in the IPCC ensemble of global coupled model simulations. J. Clim. 20 (8), 1419–1444. https://doi.org/10.1175/JCLI4066.1.

Kocaman, S., Tavus, B., Nefeslioglu, H.A., Karakas, G., Gokceoglu, C., 2020. Evaluation of floods and landslides triggered by a meteorological catastrophe (Ordu, Turkey, August 2018) using optical and radar data. ID 8830661 Geofluids 2020, 18. https://doi.org/10.1155/2020/8830661.

Lebouc, L., Payrastre, O., Bourgin, F., 2019. Reconstitution des débits de pointe des crues du 15 octobre 2018 dans le bassin de l'Aude. *Convention DGPR-IFSTTAR 2018 n° 2201132931* du 22 mai 2018 – Action 7 appui au SCHAPI. Rapport de recherche IFSTTAR, 14 p.

Lee, J.S., Pottier, E., 2009. Polarimetric Radar Imaging: From Basics to Applications. In: Optical Science and Engineering, CRC Press, Boca Raton, FL, USA, 2009.

Li, Y., Martinis, S., Wieland, M., 2019. Urban flood mapping with an active self-learning convolutional neural network based on TerraSAR-X intensity and interferometric coherence. ISPRS J. Photogramm. Remote Sens. 152, 178–191. https://doi.org/10.1016/j.isprsjprs.2019.04.014.

Liang, J., Liu, D., 2020. A local thresholding approach to flood water delineation using Sentinel-1 SAR imagery. ISPRS J. Photogramm. Remote Sens. 159, 53–62. https://doi.org/10.1016/j.isprsjprs.2019.10.017.

Martinis, S., Kuenzer, C., Wendleder, A., Huth, J., Twele, A., Roth, A., Dech, S., 2015. Comparing four operational SAR-based water and flood detection approaches. Int. J. Remote Sens. 36 (13), 3519–3543. https://doi.org/10.1080/01431161.2015.1060647.

Matgen, P., Hostache, R., Schumann, G., Pfister, L., Hoffmann, L., Savenije, H.H.G., 2011. Towards an automated SAR-based flood monitoring system: lessons learned from two case studies. Phys. Chem. Earth. 36 (7–8), 241–252. https://doi.org/10.1016/j.pce.2010.12.009.

McFeeters, S.K., 1996. The use of the Normalized Difference Water Index (NDWI) in the delineation of open water features. Int. J. Remote Sens. 17 (7), 1425–1432. https://doi.org/10.1080/01431169608948714.

Météo-France. Available online: http://pluiesextremes.meteo.fr/france-metropole/Forte s-pluies-sur-le-sud-de-la-France.

Mirsoleimani, H.R., Sahebi, M.R., Baghdadi, N., El Hajj, M., 2019. Bare soil surface moisture retrieval from sentinel-1 SAR data based on the calibrated IEM and Dubois models using neural networks. Sensors 19 (14), 3209. https://doi.org/10.3390/s19143209.

Mwaniki, M.W., Agutu, N.O., Mbaka, J.G., Ngigi, T.G., Waithaka, E.H., 2015. Landslide scar/soil erodibility mapping using Landsat TM/ETM+ bands 7 and 3 Normalized Difference Index: a case study of central region of Kenya. Appl. Geogr. 64, 108–120. https://doi.org/10.1016/j.apgeog.2015.09.009.

Nico, G., Pappalepore, M., Pasquariello, G., Refice, A., Samarelli, S., 2000. Comparison of SAR amplitude vs. coherence flood detection methods – a GIS application. Int. J. Remote Sens. 21 (8), 1619–1631. https://doi.org/10.1080/014311600209931.

Pantaleoni, E., Engel, B.A., Johannsen, C., 2007. Identifying agricultural flood damage using Landsat imagery. Precis. Agric. 8, 27–36. https://doi.org/10.1007/s11119-006-9026-5.

Petrova, Y., Westerlund, J., 2020. Fixed effects demeaning in the presence of interactive effects in treatment effects regressions and elsewhere. J. Appl. Econ. 35 (7), 960–964. https://doi.org/10.1002/jae.2790.

Plank, S., 2014. Rapid damage assessment by means of multi-temporal SAR – a comprehensive review and outlook to sentinel-1. Remote Sens. 6, 4870–4906. https://doi.org/10.3390/rs6064870.

Pléiades Days, 2014. Revue Française de Photogrammétrie et de Télédétection 209. Société Française de Photogrammétrie et de Télédétection, 2015.

Plekhov, D., Levine, E.I., 2018. Assessing the effects of severe weather events through remote sensing on Samothrace, Greece: applications for the management of cultural resources. J. Archaeolog. Sci.: Rep. 21, 810–820. https://doi.org/10.1016/j.jasrep.2018.09.002.

Pulvirenti, L., Squicciarino, G., Fiori, E., 2020. A method to automatically detect changes in multitemporal spectral indices: application to natural disaster damage assessment. Remote Sens. 12, 2681. https://doi.org/10.3390/rs12172681.

Qiu, B., Zhang, K., Tang, Z., Chen, C., Wang, Z., 2017. Developing soil indices based on brightness, darkness, and greenness to improve land surface mapping accuracy. GIScience Remote Sens. 54 (5), 759–777. https://doi.org/10.1080/15481603.2017.1328758.

Rahman, M.S., Di, L., 2017. The state of the art of spaceborne remote sensing in flood management. Nat. Hazards 85, 1223–1248. https://doi.org/10.1007/s11069-016-2601-9.

Rambour, C., Audebert, N., Koeniguer, E., Le Saux, B., Crucianu, M., Datcu, M., 2020. Flood detection in time series of optical and SAR images. In: International Archives of the Photogrammetry, Remote Sensing and Spatial Information Sciences. https://doi.org/10.5194/isprs-archives-XLIII-B2-2020-1343-2020.

Rasmussen, C.E., Williams, C.K.I., 2006. Gaussian Processes for Machine Learning. The MIT Press, 2006. ISBN 0-262-18253-X.

Robertson, L.D., King, D.J., 2011. Comparison of pixel- and object-based classification in land cover change mapping. Int. J. Remote Sens. 32 (6), 1505–1529. https://doi.org/10.1080/01431160903571791.

Saha, S., Bovolo, F., Bruzzone, L., 2019. Unsupervised deep change vector analysis for multiple-change detection in VHR images. IEEE Trans. Geosci. Remote Sens. 57 (6), 3677–3693. https://doi.org/10.1109/TGRS.2018.2886643.

Santi, E., Dabboor, M., Pettinato, S., Paloscia, S., 2019. Combining machine learning and compact polarimetry for estimating soil moisture from C-band SAR data. Remote Sens. 11 (20), 2451. https://doi.org/10.3390/rs11202451.

Sepuru, T.K., Dube, T., 2018. An appraisal on the progress of remote sensing applications in soil erosion mapping and monitoring. Remote Sens. Appl.: Soc. Environ. 9, 1–9. https://doi.org/10.1016/j.rsase.2017.- 10.005.

Sheng, Y., Gong, P., Xiao, Q., 2001. Quantitative dynamic flood monitoring with NOAA AVHRR. Int. J. Remote Sens. 22 (9), 1709–1724. https://doi.org/10.1080/01431160118481.

Singha, M., Dong, J., Sarmah, S., You, N., Zhou, Y., Zhang, G., Doughty, R., Xiao, X., 2020. Identifying floods and flood-affected paddy rice fields in Bangladesh based on Sentinel-1 imagery and Google Earth Engine. ISPRS J. Photogramm. Remote Sens. 166, 278–293. https://doi.org/10.1016/j.isprsjprs.2020.06.011.

SNAP v7.0, 2018. S1TBX – ESA Sentinel -1 Toolbox. http://step.esa.int.

Swain, K.C., Singha, C., Nayak, L., 2020. Flood susceptibility mapping through the GIS-AHP technique using the cloud. ISPRS Int. J. Geo-Inf. 9 (12), 720. https://doi.org/10.3390/ijgi9120720.

Tavus, B., Kocaman, S., Gokceoglu, C., 2021. Assessment of flooded areas caused by a dam break (Sardoba dam, Uzbekistan). Int. Arch. Photogramm. Remote Sens. Spatial Inf. Sci. XLIII-B3-2021, 291–297. https://doi.org/10.5194/isprs-archives-XLIII-B3-2021-291-2021.

Twele, A., Cao, W., Plank, S., Martinis, S., 2016. Sentinel-1-based flood mapping: a fully automated processing chain. Int. J. Remote Sens. 37 (13), 2990–3004. https://doi.org/10.1080/01431161.2016.1192304.

Uddin, K., Matin, M.A., Meyer, F.J., 2019. Operational flood mapping using multi-temporal sentinel-1 SAR images: a case study from Bangladesh. Remote Sens. 11, 1581. https://doi.org/10.3390/rs11131581.

Wagner, W., Lemoine, G., Rott, H., 1999. A method for estimating soil moisture from ERS scatterometer and soil data. Remote Sens. Environ. 70 (2), 191–207. https://doi.org/10.1016/S0034-4257(99)00036-X.

Wang, X., Jiang, D., Lang, X., 2017. Future extreme climate changes linked to global warming intensity. Sci. Bullet. 62 (24), 1673–1680. https://doi.org/10.1016/j.scib.2017.11.004.

Yamagata, Y., Akiyama, T., 1988. Flood damage analysis using multitemporal Landsat Thematic Mapper data. Int. J. Remote Sens. 9 (3), 503–514. https://doi.org/10.1080/01431168808954871.

Yésou, H., Clandillon, S., Allenbach, B., Bestault, C., de Fraipont, P., Inglada, J., Favard, J.C., 2003. A constellation of advantages with SPOT SWIR and VHR SPOT 5 data for flood extent mapping during the September 2002 Gard event (France). IGARSS 2003. In: 2003 IEEE International Geoscience and Remote Sensing Symposium. Proceedings (IEEE Cat. No.03CH37477), vol. 1, 2003, pp. 567–569. https://doi.org/10.1109/IGARSS.2003.1293844.

Yésou, H., Escudier, A., Battiston, S., Dardillac, J.-Y., Clandillon, S., Uribe, C., Caspard, M., Giraud, H., Maxant, J., Durand, A., Fellah, K., Studer, M., Huber, C., Philippoteaux, L., de Fraipont, P., Fontannaz, D., 2015a. Exploitation de l'imagerie Pléiades-THR en cartographie réactive suite à des catastrophes naturelles ayant affecté le territoire français en 2013. Revue Française De Photogrammétrie Et De Télédétection 209, 39–45.

Yésou, H., Chastanet, P., Maxant, J., Huber, C., Clandillon, S., Battiston, S., Proy, C., de Fraipont, P., 2015b. Contribution de l'imagerie Pléiades à la cartographie rapide des dégâts suite à des catastrophes majeures: retours d'expériences après deux ans d'actions de cartographie rapide localisées en Asie, en Afrique, en Europe et aux Caraïbes. Revue Française De Photogrammétrie Et De Télédétection 209, 81–87.

Zribi, M., Saux-Picart, S., André, C., Descroix, L., Ottlé, O., Kallel, A., 2007. Soil moisture mapping based on ARSAR/ENVISAT radar data over a sahelian site. Int. J. Remote Sens. 28 (16), 3547–3565. https://doi.org/10.1080/-01431160601009680.